3D PRINTED BIOCATALYTIC SILICA HYDROGEL FLOW-THROUGH REACTOR FOR ATRAZINE DEGRADATION

A THESIS
SUBMITTED TO THE FACULTY OF
UNIVERSITY OF MINNESOTA
BY

RYAN S. HAN

IN PARTIAL FULFILLMENT OF THE REQUIREMENTS
FOR THE DEGREE OF
MASTER OF SCIENCE

ADVISOR: DR. MICHAEL C. McALPINE

JUNE 2017

Acknowledgements

Throughout this thesis work, many individuals and specific labs have helped me grow through learning and experience.

First, I would like to thank my advisor, Dr. Michael McAlpine, for his continued support, insight, and guidance throughout my Master's thesis.

Next, I thank my examining committee: Dr. Alptekin Aksan and Dr. Paige Novak, for their time and insight they gave for review of my thesis and defense.

To my fellow labmates within the McAlpine Research Group, I express my appreciation for all of our discussions and their insight to overcome complications that arose within my research project. Specifically, I would like to thank lubility.

I would like to express my gratitude to my collaborators: Dr. Baris Mutlu and Jonathan Sakkos for their continued insight at every step of this project as well as Sujin Yeom for the growth of the bacteria used in this project as well as many detailed discussions on the fundamentals of microbiology.

Additionally, I would like to thank Dr. Larry Wackett for his support in determining direction in biological incorporation into the 3D printed ink. Again, I would like to thank Dr. Alptekin Aksan for his input on the encapsulation material used in this thesis work.

Dr. Thomas Pengo of the University of Minnesota Informatics Institute, developed the MATLAB code for the χ^2 distribution analysis, and I would like to thank him for this input and support.

In conducting my simulation work, Dr. John Gorman was extremely helpful in the design of the simulation model as well as simulation logistics. I appreciate all of the extra time and insight Dr. Gorman provided me.

For the collection of gelation time and mechanical properties, I would like to thank the services of the Polymer Characterization Facility. Additionally, I would like to thank the services of the University of Minnesota - University Imaging Centers, http://uic.umn.edu, for training and use on the Nikon A1Rsi Confocal Microscope that was used for the fluorescent imaging.

In addition to my research support, I would like to thank those who have supported me as a teaching assistant at the University of Minnesota, for the Basic Mechanical Measurements course. Dr. Peter McMurry, Dr. Peter Bruggeman, and Dr. Chris Hogan all were vital in my development as a TA. Also, I would like to thank Dr. Bernard Olson for his help in providing TA lab support throughout my time as a TA.

Lastly, I am grateful for the love and support I have received from my family: my parents, John and Jane Han, as well as my brother and sister-in-law, Jason and Lauren Han, and my girlfriend, Kallie Delveaux.

Dedication

This thesis is dedicated to my family and in loving memory of Juanita Ward, Robert E. Ward, and Dr. Chung-Mao Han.

Abstract

One of the most heavily used herbicides in the world, atrazine, provides a serious environmental challenge that we face presently. Atrazine has been consistently applied to farms due to its proven ability to remove broadleaf weeds, allowing for increased yields of corn crops, which is necessary to feed an ever-growing world population. However advantageous the use of atrazine is, toxic effects have been identified when humans ingest atrazine. Also, the high mobility of atrazine during run-off events after application to fields allows atrazine to be easily incorporated into water systems around agricultural land, creating a large-scale health and environmental problem as the increased atrazine concentrations negatively impact human health when ingested as well as ecological disturbances when affecting local algal communities.

The presented work investigates the application of 3D printing as an approach to solving this significant problem. We hypothesize that with direct-write 3D printing of biologically active, printed materials to perform the bioremediation of atrazine, may enhance bioremediation capacity compared to conventional methods by utilizing the near limitless rapid design flexibility intrinsic to 3D printing to allow fabrication of structures with high surface area to volume ratio (SA:V), yielding lower diffusion length scales that allow improved encapsulated biocatalyst usage.

We introduce a novel 3D printing method to produce application specific complex 3D geometries from a sol-gel based silica material with encapsulated biocatalysts. To produce a bioactive material with the incorporation of biocatalysts, silica hydrogel formed through a sol-gel process was used as the ink base. *E. coli* genetically engineered

to overexpress the AtzA enzyme, which degrades the toxic herbicide atrazine to the non-toxic compound hydroxyatrazine, were encapsulated within the silica-based ink. This process leverages the strong mechanical properties, high chemical transport properties, and biocompatibility of the silica base material along with the full material customization, precision in spatial deposition, and design flexibility intrinsic to the 3D printing process to overcome obstacles that hinder the use of bioactive materials within conventional 3D printers (material constraints and biologically deadly processing).

The developed 3D printer ink was characterized in terms of gelation kinetics, mechanical properties, cell distribution, and degradation capability. Results confirmed that the 3D printed AtzA biocatalysts sustained biodegradation ability through the removal of atrazine and production of hydroxyatrazine through batch reactor experiments. High SA:V geometries produced through 3D printing also showed improved degradation efficiency by encapsulated biocatalysts. This allowed for an advantage over previously presented work because by providing high SA:V structures, the atrazine did not have to diffuse over long length scales until it was biotransformed within a bacterial cell. Structures with low SA:V were shown to decrease in degradation efficiency because as the atrazine concentration gradient decreased, only the cells closer to the surface would perform the biotransformation of atrazine, the cells located more centrally would not contribute to the degradation. Therefore, with a decrease in diffusion length to all encapsulated biocatalysts, the overall function of the encapsulated population as the concentration of atrazine dropped would be improved over past methods. Additionally, a flow-through bioreactor was designed, simulated, and experimentally

tested. ANSYS reaction-flow simulations were completed to determine experimental flow rates necessary to positively identify atrazine degradation in the flow-through bioreactor. Finally, atrazine degradation was proven in flow-through experiments at an inlet flowrate of 1 ml/min. Observed atrazine degradation equated to 15 ± 5% of overall inlet concentration atrazine. Through this work, we have shown as a proof of concept that 3D printed silica-encapsulated biocatalysts sustain the function to degrade an environmental pollutant. This work may be expanded further via the incorporation of multiple types of biocatalysts encapsulated in an organized pattern (multiple different 3D printer inks printed in a designed pattern) that enhances biotransformation and transport of products between the multiple biocatalysts. In addition, this work may be applied to advance fields where complex geometries of encapsulated biocatalysts are necessitated, which may include the fields of pharmaceutical, medical, environmental, and materials science.

Table of Contents

List of Figures

CHAPTER 1

Introduction

1.1 Project Motivation & Objective

In order to produce quantities of food necessary to support the expanding global population, atrazine, a triazine-class herbicide, has been widely applied on farms around the world.[1] Atrazine may be applied pre- or post-emergence of weeds, which allows farmers to decrease tilling. With less tilling being conducted on farms, this has led to lowering soil erosion impacts, increased soil moisture conservation, improved organic matter retention, and a decrease in fuel usage.[1,2] Atrazine works through disrupting the photosynthetic process within a broad range of weeds.[3] Corn, one of the main crops that atrazine is widely used for, has an internal protection system that detoxifies atrazine prior to the photosynthesis inhibition affecting the corn plant.[4] Because of the ability to cripple weed growth within cornfields and promote economic enhancements for farmers, atrazine has been widely used around the world since its development in the 1950s.[1]

However beneficial atrazine usage is to high yield corn crops, there are numerous environmental and health concerns that oppose the use of this herbicide, leading to the herbicide being banned in Europe in 2003.[5] These concerns are intensified due to the amount of atrazine now found in local aquifers and drinking water.[6-8] Atrazine has high solubility in water and persistence in the soil, allowing retention for months as well as having the ability to be carried away from farms during run-off events.[9-11] When atrazine is transported from its point of application, problems arise. Human impacts have been

identified in past studies where atrazine has been shown to negatively affect the reproductive system, and cause liver, kidney, and heart damage in humans.[12] Further effects are difficult to determine, but there has been evidence to show possible connections between atrazine exposure and an increase risk of breast, prostate, and stomach cancers.[13-15] Additionally, atrazine has been shown to have some effect on hormone levels, immune function, and the nervous system in animals.[16,17] Environmental impacts of the introduction of atrazine into rivers, ponds, and lakes include diminishing algal and macrophyte communities through photosynthetic pathway disruption, which drastically affect all aquatic life through lower dissolved oxygen levels, higher turbidity levels, and a decrease in pH.[18] Other environmental impacts include developmental abnormalities in frogs and lower the survivability of exposed salmon.[19,20]

Because of the high mobility of atrazine and subsequent harm to human health and the environment, numerous technologies have been developed for the removal and remediation of atrazine. These technologies include chemical degradation, incineration, adsorptions, phytoremediation, and bioremediation.[21-26] The U.S. EPA has determined that the best technology for removing atrazine from drinking water is through adsorption onto activated carbon structures, but this only provides a disposable solution as the carbon substrate must be incinerated or disposed of after being used.[21,23,26]

Recently, attention has shifted to bioremediation of atrazine as new biocatalysts have been identified that carry out the reaction to dechlorinate atrazine.[27-29] In order to improve bioremediation as a viable option for atrazine removal in drinking water, one main factor of popular concern is protecting the bacteria from wash-out into the drinking

water source, which can be improved through immobilization or encapsulation techniques.[30] When grown as biofilms there may still be loss of biocatalyst, which would be undesirable. Biocatalysts have been shown to be encapsulated in numerous materials including alginate, silica, and nanofibers.[31-33] With encapsulation, advantages over free cell bioremediation include increased retention of biocatalysts leading to further sustained remediation ability, biocatalyst protection from wash-out and substrate inhibitory effects, and increased resistance to chemical and biological factors found in the remediation environment.[30,34]

Silica encapsulation has been proven to be one of the most promising immobilization techniques for bioremediation purposes. Silica sol-gel encapsulation allows a room temperature, rapid encapsulation of cells within a rigid, but porous structure that is neither a food source nor toxic to the encapsulated biocatalysts (enzymes or whole cells).[35] The sol-gel process is based around the polycondensation of a hydrolyzed silicon alkoxide precursor, and may be expanded to a mixture between the alkoxide precursor and colloidal suspensions of silica nanoparticles.[36] Through variation in precursor ratios, the silica hydrogel may be tuned and optimized for a certain application through modified mechanical properties.[26]

3D printing has been a technology and industry that has grown rapidly in the past 10 years.[37] A few examples of fields where 3D printing has displayed progress include rapid prototyping, biotechnology, customized medical devices, and bionic devices.[37-42] 3D printing of environmentally sustainable materials has yet to be developed as printing of bacteria is in its beginning.[43,44] Other 3D printing work relating to microorganisms

solely focuses on the localization and segregation of bacteria to study bacterial community interactions.[45]

The advantages of direct-write 3D printing allow for fully customized materials, complete integration of multi-material production, precise spatial positioning of deposited materials, and rapid design and production of complex 3D shapes.[42] Conventional 3D printing processes have many constraints that hinder development of biologically infused materials to be used. These include low material flexibility, high temperature processing, and UV light or laser use for material cross-linking.[46,47]

Similar to medical applications utilizing 3D printing for anatomically unique form factors and application areas, 3D printing of sustainable materials may be rapidly designed and produced for unique applications requiring refined and specific geometries that further optimize the bioremediation potential. Given different biocatalysts utilized in the bioink, variations of bioreactors may be produced to tackle numerous environmental challenges such as pollutant remediation, energy production, and ecological stability. Each of these applications would benefit from custom design and production in order to optimize spatial relation between environmental factors, biocatalysts, and supporting materials, which is possible with 3D printing. For example, if the product of one biotransformation is toxic as well as the initial compound, another biocatalyst may be printed in a location so as to increase the transfer of the product to the new bacterial strain where it may be then converted to the non-toxic compound.

With the ability to rapidly design and produce sustainable bioactive materials from sol-gel silica with near limitless design constraints, this method outperforms

previous works of silica encapsulated AtzA biocatalysts that utilize molds for shaping of the gel during synthesis. This is because the use of molds limit the possible produced forms and redesigns of the molds would take multiple steps of designing the desired shape, designing the mold, printing the mold, filling the mold, and allowing the mold to cure.[48] In addition, with 3D printing, structures with high surface area to volume ratios (SA:V) may be fabricated, which can decrease diffusion lengths for the atrazine, thereby increasing the overall degradation efficiency to overcome the capability presented in previous works.

The goal of this work is to develop a method to 3D print bioactive materials for enhanced atrazine removal. Because direct-write 3D printing allows for complete material customization, this permits the realization of tuned and optimized ink comprised of sol-gel silica with encapsulated biocatalysts. Design and production of high SA:V structures allows for all encapsulated biocatalysts to be utilized for full bioremediation capability, therefore outperforming previously presented molded silica encapsulated biocatalysts for atrazine removal. From this work, a new field of 3D printing may be opened for further advances that may contribute new and innovative solutions to grand challenges that harm populations around the world.

1.2 Related Works

Silica encapsulation of biocatalysts has been a proven protection method for biocatalysts over the past couple decades.[32] The enzyme, AtzA, has been proven to carry out degradation of atrazine while encapsulated within silica-based sol-gel materials.[26,49,50] Additionally, in terms of 3D printing of biological materials, numerous studies have

shown the ability to print cells and tissues while sustaining function within the live printed entities.[41,51]

However, silica encapsulation of biocatalysts has yet to be used in 3D printing. Overall, 3D printing of silica materials has only recently been realized. Kotz et al. provided stereolithography 3D printing of transparent, fused silica glass.[52] This work allowed the first use of 3D printing with silica glass materials, but is not applicable to bioremediation due to the printing and processing method. First, the resin used in this stereolithography 3D printing is cross-linked via a UV curable monomer, which would result in large-scale cell death. Secondly, to fuse the printed layers together, heat was applied at 1300 °C. This temperature may never be used around biocatalysts without enzyme denaturation and complete destruction of the cell structure. Furthermore, sol-gel inks have been used in 3D printing previously by Duoss et al, but the material was based off of polyvinyl-pyrrolidone (PVP).[46] Again, the printed ink is not biocompatible as the ink must be post-processed at a temperature of 715 °C for 1 hour.

To this date, only one study has been published regarding 3D printing with bacteria.[43] In this work, Lehner et al. printed *E. coli* mixed with a dissolved alginate solution that solidified upon contact with a calcium ion-coated substrate. With this process, the printing of subsequent layers necessitated the diffusion of calcium ions from the printing substrate across previously printed layers in order to adequately gel the printed bioink. To test bioactivity, the *E. coli* were transformed with an SB101 plasmid that encoded for the rhamnose-inducible red fluorescent protein (RFP). Therefore, when the printed gel containing the RFP expressing *E. coli* was printed on a gel containing

rhamnose, the gels turned red in color. This allowed Lehner et al. to confirm metabolic activity of post-3D printed bioinks.

1.3 Project Outline

In order to adequately capture the scope of the presented research, the following project flow map was developed (Figure 1).

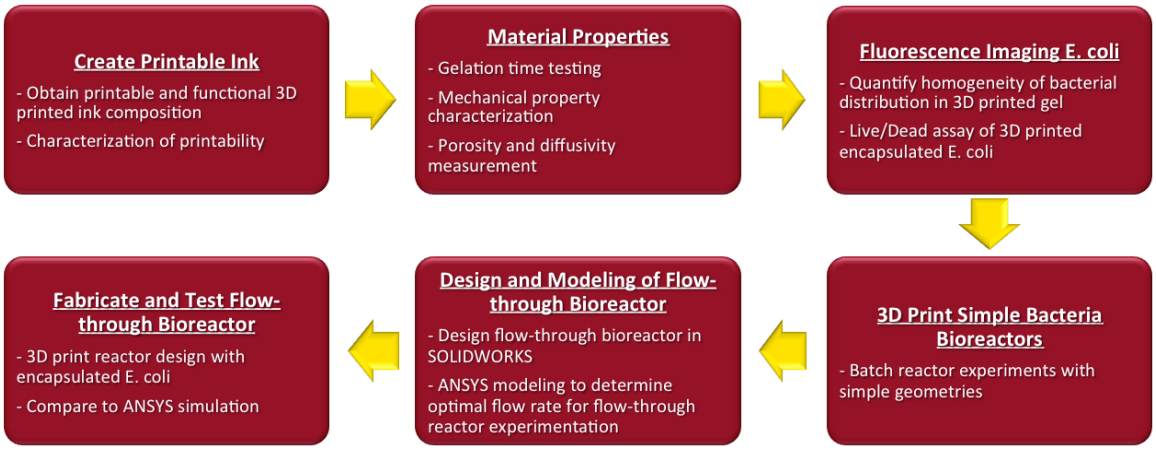

Figure 1. Project flow map detailing research milestones.

First, the ink was developed via numerous design iterations with the intent to satisfy both printability and functionality specifications as described previously. After the printability was characterized through simple printed structures, the material properties were investigated to quantify the gelation kinetics, intrinsic mechanical properties, and porosity of the developed 3D printer ink. In addition, the diffusivity of atrazine through the silica hydrogel was measured. The porosity and diffusivity were variable inputs into the ANSYS modeling later in the project. To finalize characterization of the 3D printer ink, bacteria were introduced into the ink to measure the homogeneity of the bacterial distribution along with the bacterial viability within printed structures. This was

conducted via fluorescent microscopy utilizing both green fluorescent protein (GFP) expressing *E. coli* for bacterial distribution and atrazine chlorohydrolase (AtzA) expressing *E. coli* for viability measurements through Live / Dead assays. After the ink was fully characterized, the functionality of 3D printed structures with encapsulated biocatalysts was tested in batch experiments to measure effectiveness of atrazine degradation. Once functionality of the 3D printed structures was confirmed, the final phase of the project commenced, starting with design of the flow-through bioreactor. A flow-through bioreactor was chosen based on the ability of 3D printing to produce complex geometries that could effectively increase efficiency of degradation per bacterium from a high surface area to volume ratio (SA:V). The SOLIDWORKS design was inputted into ANSYS for fluid and degradation modeling. Finally, the designed structure was printed and flow-through degradation experiments were completed. The experimental results were compared with the simulation to determine the accuracy of the simulation.

CHAPTER 2

Research Background

2.1 Bioremediation of Atrazine

Until the mid-1980s, atrazine was assumed to be very difficult to degrade through biochemical pathways.[53] Today, there are numerous strains of bacteria are known that have the ability to degrade atrazine to hydroxyatrazine.[28,49] *Pseudomonas* sp. strain ADP was one of the first strains that was isolated and found to have atrazine degradation ability.[53] The *Pseudomonas* sp. strain ADP was isolated from an atrazine spill where the local microbiota developed a multistage-catabolic pathway to degrade atrazine to ammonia and carbon dioxide.[54] The full atrazine degradation pathway is provided below in Figure 2.

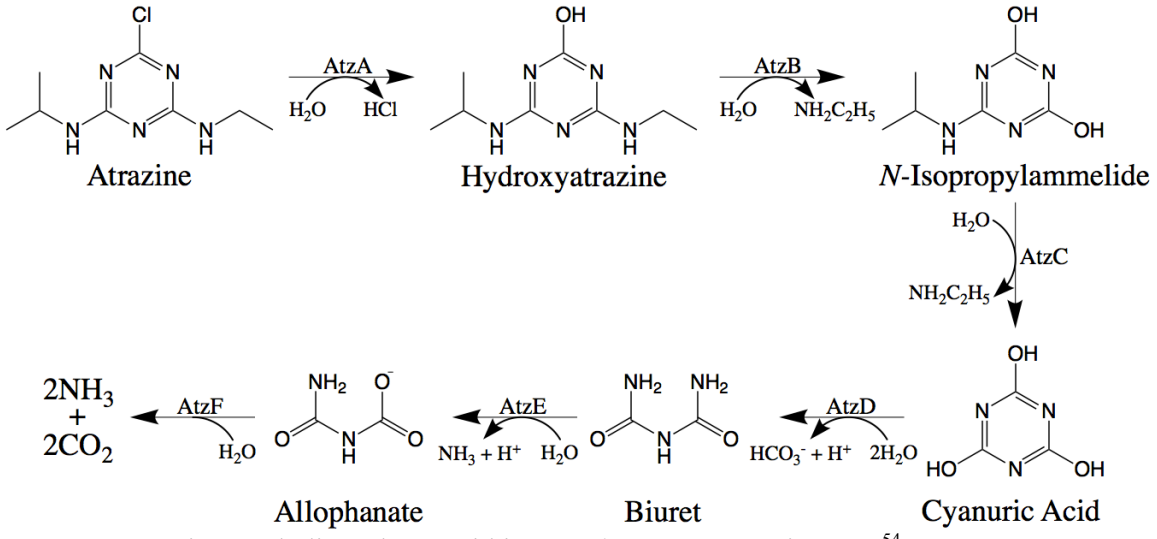

Figure 2. Atrazine catabolic pathway within *Pseudomonas* sp. strain ADP.[54]

The first step of the catabolic pathway, carried out by the AtzA enzyme, biotransformed atrazine to hydroxyatrazine. This is the most important step, as the toxic

compound, atrazine, is dechlorinated to hydroxyatrazine, a non-toxic compound.[3] Additionally, Wackett et al. have described the decrease in environmental implications once atrazine has been converted to hydroxyatrazine.[3] Because of this initial step being the most important, further studies moved to clone the genes that encode for the AtzA enzyme from the *Pseudomonas* sp. strain ADP into *E. coli* DH5α.[55] To further the degradation potential of atrazine to hydroxyatrazine, the *E. coli* were specifically engineered to overexpress the AtzA enzyme.[56] Also, *E. coli* provide a cheap solution for bioremediation due to their inexpensive nature from growth protocols being fully developed, producing consistent large yields.[49] Due to this, genetically engineered *E. coli* DH5α represent a bioremediation agent with high potential.

2.2 Bioencapsulation

In order for bacteria to be utilized as a remediation solution within an aqueous environment, the cells must first be immobilized so as to not lose degradation efficiency through a wash-out event where the cells are removed from the reactor environment.[34] Immobilization techniques range from flocculation, adsorption, bonding to carrier, cross-linking between cells, encapsulation within a polymer-gel, and entrapment within a matrix and advantages of these techniques include[30,57]:

- Increased metabolic activity
- Protection from environmental stresses such as toxic compounds, predation, and thermal and chemical instability
- Ease of storage, transport, and application of the biocatalysts

- Increased retention of biocatalysts for lengthened degradation activity as well as improved public safety

The most suitable immobilization method for bioremediation purposes is encapsulation of biocatalysts within a polymer-gel. Both natural and synthetic polymers have been used. Natural polymers for bioencapsulation include alginate, agarose, chitosan, cellulose, collage, and xanthan gum while synthetic polymers for encapsulation include poly(ethylene glycol) (PEG), polyvinyl alcohol (PVA), polyurethane (PU), poly(ether-sulfone) (PES), polypropylene (PP), sodium polystyrene sulfate (PSS), and polyacrylate poly(acrylonitrile-sodium methallylsulfonate).[58] Both natural and synthetic polymers provide advantages over one another. Natural polymers are typically biocompatible, but mechanically weak and may be biodegradable, allowing release of the biocatalysts.[59] Synthetic polymers tend to have high purity when produced leading to constant properties between batches, but polymerization may necessitate the use of harsh solvents that would kill the encapsulated biocatalysts as well as other biocompatibility concerns.[58]

Another encapsulation pathway that has produced numerous advantages over the previously listed materials is silica.[34] Silica hydrogels produced through the sol-gel method have been shown to allow improved function of encapsulated biocatalysts.[60,61] Silica encapsulation provides high retention of bacteria through improved mechanical properties while ensuring high mobility of solutes through the gel via large pore sizes.[62] In addition, the encapsulation process is conducted at mild conditions, improving retention of cell viability and function.[63]

2.3 Silica Sol-Gel Chemistry

The sol-gel process is one where a sol, a liquid suspension of solid particles in the size range of 1 nm to 1 μm, undergoes a polycondensation reaction to produce a three-dimensional interconnected network to form a gel (diphasic material where a solid structure encapsulates a solvent).[64] Through the sol-gel process, high material purity and homogeneity may be achieved through a low temperature process.[36] Through the versatility of sol-gel materials, produced gels may easily be formed in various physical forms and their mechanical properties (strength, porosity) can be tuned through varied sol materials and processing steps.[64] One method to make silica sol-gel materials has been through the hydrolysis and subsequent polycondensation of alkoxide precursors.[36] The hydrolysis of one common alkoxide precursor is given below in Figure 3.

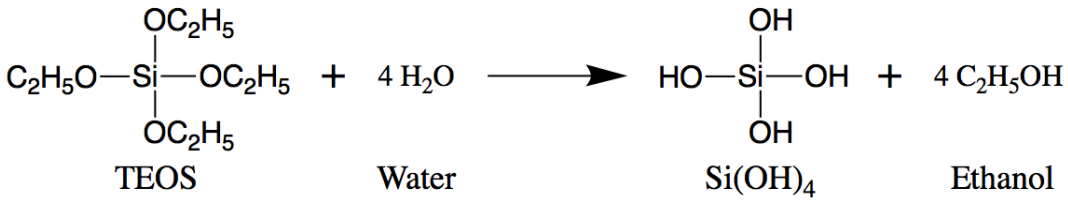

Figure 3. Hydrolysis of the sol-gel alkoxide precursor, TEOS.

After the alkoxide, tetraethyl orthosilicate (TEOS) represented in Figure 3, has been hydrolyzed, it may undergo condensation reactions (Figure 4 and Figure 5) to form the silica hydrogel.

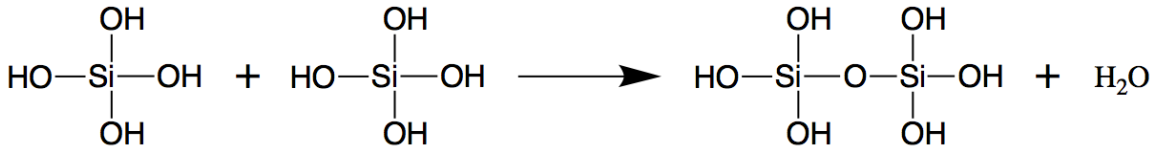

Figure 4. Sol-gel condensation reaction between hydrated silica tetrahedra.

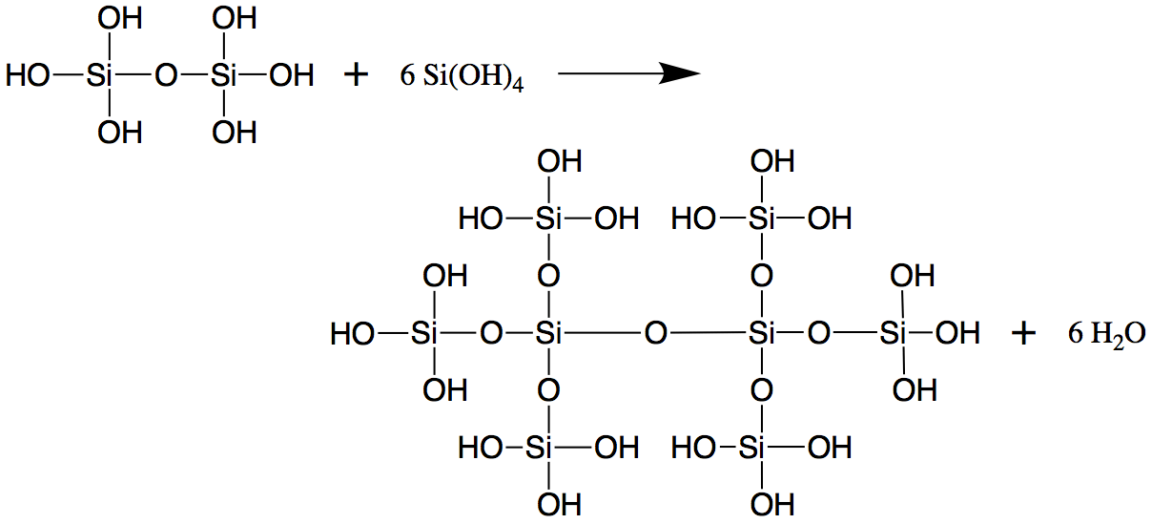

Figure 5. Sol-gel polycondensation reaction to form silica-based gel.

Because of the small size of the monomer used in this reaction, the final product is a very strongly bound structure, allowing for enhanced mechanical properties. Recently, research has been conducted to incorporate silica nanoparticles with the silicon alkoxide precursors, allowing the alkoxide to act as a cross-linker between the much larger nanoparticles.[65] Through the variation in nanoparticle size, it was observed that the diffusivity of the developed silica gel could be tuned for different applications.[26]

CHAPTER 3

Conducted Research

3.1 Overview

Here, we introduce a novel technique to spatially control encapsulated biocatalysts via direct-write 3D printing within a silica hydrogel for function in bioremediation of the EPA regulated herbicide, atrazine. In this work, we show 1) 3D printing of silica-based sol-gel materials, 2) active bioremediation within 3D printed structures, 3) enhanced bioremediation efficiency through high surface area to volume (SA:V) ratio geometries, and 4) both computation flow-reaction modeling and experimental results of bioremediation within flow-through bioreactors with complex 3D printed geometries containing encapsulated functioning biocatalysts. Figure 6 illustrates our overall concept to design and fabricate a silica-based flow-through bioreactor. The 3D printed spiral structure was produced in a one-pot synthesis step with dual extrusion heads that were synced within the G-code for defining the motion of the spatial positioning system.

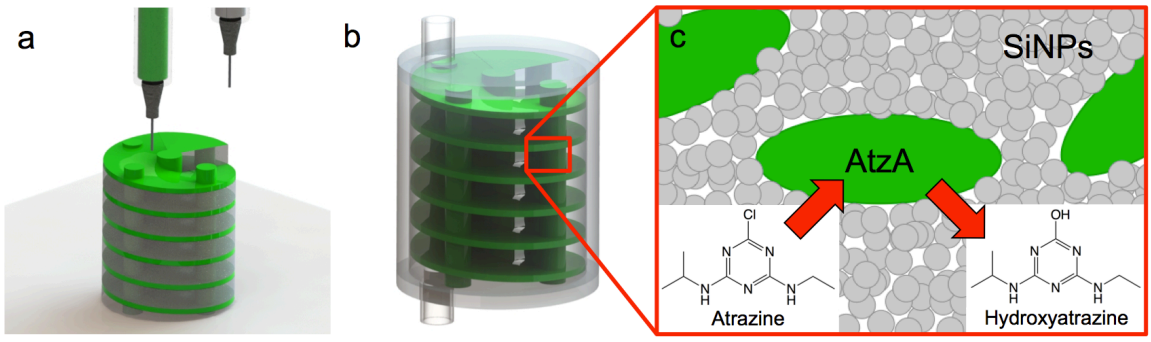

Figure 6. 3D printed bioremediation capsule: a) 3D printing of bioactive silica hydrogel (green) with support structure (transparent grey), b) assembled capsule for flow-through bioremediation, and c) functional schematic of SiNP encapsulated biocatalysts for atrazine degradation.

3.2 Method for 3D Printing of Silica Sol-Gel Material

In order to develop the 3D printed structure, formulation and tuning of the ink composition was necessary to create ink that first, allowed controlled fluid deposition during printing, second, formed a rigid structure post deposition, and third, allowed biocatalysts to sustain bioremediation function after printing. The developed ink was composed of a colloidal silica nanoparticle (SiNP) suspension (Ludox HS-40, Sigma Aldrich), polyacrylamide (PAM) (average M_n=150,000, Sigma Aldrich), hydrolyzed tetraethyl orthosilicate (TEOS) (Sigma Aldrich), glycerol (Sigma Aldrich), and phosphate buffered saline (PBS). The SiNPs, depicted in Figure 6c would be cross-linked by the TEOS within the sol-gel transition, encapsulating the biocatalysts within the hydrogel.

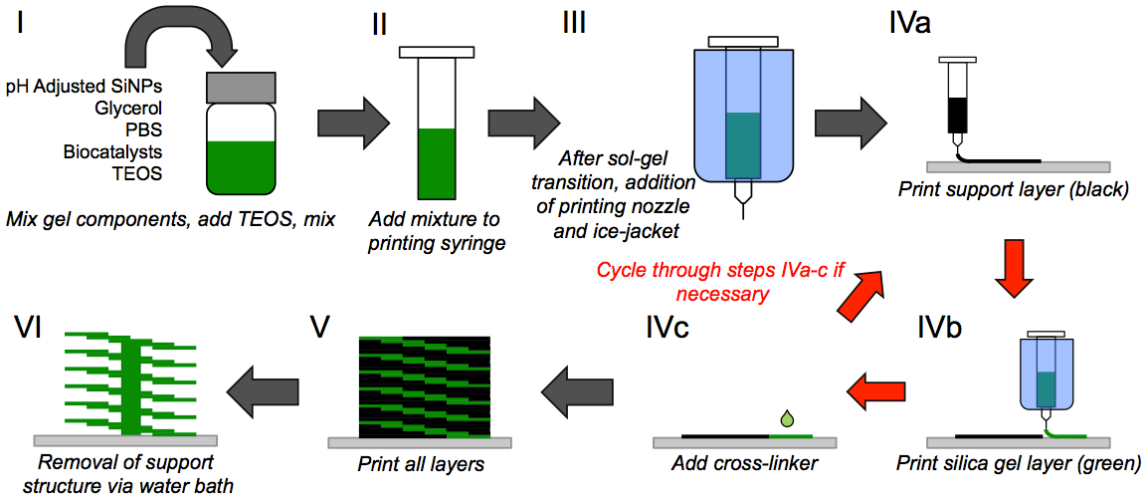

Figure 7. 3D printing process schematic: ink I) preparation and II) addition to 3D printing syringe prior to sol-gel transition. Post sol-gel transition, III) application of syringe tip and implementation of ice-jacket for aging stabilization. Controlled printing of IVa) water soluble support structure (black) and IVb) silica encapsulated biocatalysts (green) with IVc) subsequent TEOS added to silica ink. V) Structure after successful 3D printing and VI) 3D printed structure after removal of water soluble support structure.

A novel 3D printing process was developed in order to control the chemical kinetics of the sol-gel polycondensation reaction as well as provide high fidelity 3D

prints. Figure 7 demonstrates the 3D printing process. First, TEOS was hydrolyzed via stirring with water and hydrochloric acid (HCl) for 2 hrs when mixed in a 1:5.3:0.0013 M ratio of TEOS:H2O:HCl. PAM was added to the SiNP colloidal suspension at 2 wt% and stirred for 2 hrs. The SiNP-PAM suspension was then pH adjusted to pH=7.0 through addition of 1.0 M hydrochloric acid (HCl). The pH adjusted SiNP-PAM suspension was then vortex mixed with PBS and the mixture was used to re-suspend the *E. coli.* Two types of *E. coli* were used in this study that expressed 1) green fluorescent protein (GFP) and 2) the atrazine-degrading enzyme, atrazine chlorohydrolase (AtzA). Glycerol was then mixed in with the other gel components, prior to addition of the hydrolyzed TEOS. Hydrolyzed TEOS was then added so that the overall makeup of the ink was composed of a ratio of 78.57 : 3.93 : 15.00 : 2.50 (SiNP : TEOS : Glycerol : PBS). After addition of the hydrolyzed TEOS, the mixture was vortex mixed (Step I) and the mixture was added to the 3D printing syringe (Step II). Once the sol-gel transition had begun, the ice-jacket was introduced to cool the mixture (Step III), effectively slowing, and halting, the polycondensation reaction to hold the viscoelastic properties of the ink constant throughout the printing time. For designs necessitating support structure, a water-soluble material, Pluronic F-127 (Sigma Aldrich), was mixed with ultrapure water to a 30 wt% composition (Step IVa). If no support material was needed for structural integrity throughout the printing time, two layers of the developed silica gel were printed consecutively, and the appropriate amount of TEOS was added to increase volumetric composition of the ink to 11.5% TEOS (Steps IVb-c). After the TEOS was added, printing was paused of 2 minutes to allow absorption into the printed structure for

reaction and strengthening. Also, if printing commenced too soon after addition of the TEOS to the previous layers, the surface adhesion between the previous layer and the extruded silica gel would be poor as the liquid TEOS would separate the top layer and the printed ink, decreasing printing quality. The process of pausing printing for 2 minutes between certain layers of printing was not observed in structures requiring support structure as the TEOS was added and absorbed during the printing of the support structure. After all layers were printed, support material, if used, was removed by introduction of the printed structure to a PBS bath for time appropriate for the structure design and amount of support material incorporated (Steps V & VI).

This process allowed adequate control over the chemical transition so that the sol-gel process was ideal for 3D printing. Without control, the sol-gel transition may occur quickly, where the liquid mixture undergoes a rapid polycondensation reaction, forming a strong gel in a short amount of time. To guarantee printing quality, the ink must have some level of an internal structure to allow for developed printing patterns to be held by the deposited ink, but fluid enough to ensure extrusion through the printing nozzle can be completed at low pressures as to protect the biocatalysts. In order to overcome these issues, printing quality was improved via an environmental stabilization jacket applied to the printing syringe that held the ink near 0 °C so that the silica sol-gel reaction was halted when desired. This allowed for sustained fluid properties throughout the length of the print time after the ink had undergone the beginning of the polycondensation reaction so that the printed ink was structurally sound. Additional TEOS was added to the printed

ink to further strengthen the printed structure that increased the proportion of TEOS to 11.5% of the total volume.

3.3 Characterization of Silica Sol-Gel 3D Printer Ink

Characterization of the ink was conducted in order to determine sol-gel kinetics via the gelation time, t_g. From this characterization, it was determined when the environmental jacket would be applied to augment the gelation kinetics favorably for printing quality. A time-sweep was conducted on a rotational rheometer (TA Instruments) to determine the point of gelation according to published methods where the gelation time was given by the intersection of *tan(δ)* of multiple frequency oscillation series.[66]

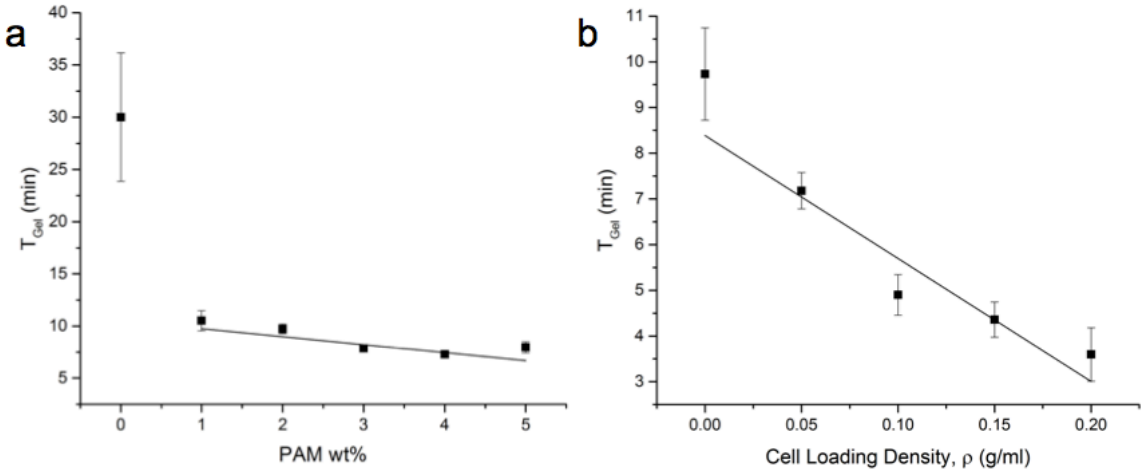

Figure 8. Gelation time characterization of varied gel compositions: gelation time dependence on a) PAM weight percent as mixed with SiNPs and b) cell loading density. Error bars represent standard deviation with n=5.

Two trials were completed to investigate the effect of PAM wt% when mixed with SiNPs (Figure 8a) as well as the effect of *ρ,* cell loading of GFP expressing *E. coli*, (Figure 8b) on gelation time. The PAM wt% trials were completed without cell loading and the cell loading density trials were completed with 2 wt% PAM as mixed with the

SiNP colloidal suspension. It was apparent that both variables provide negative correlations with the gelation time. For the addition of polyacrylamide, this can be attributed to the effect of chemical templating from hydrogen bonding between the hydroxyl functional groups on the SiNPs and the amino functional groups on the PAM chains.[67,68] This templating of the SiNPs on the PAM chains causes the formation of a loose structure within the mixture prior to TEOS addition, leading to a decrease in open hydroxyl groups when the TEOS is added, providing for gelation to be completed at a faster rate. Similarly, as ρ increases, the gelation time decreases. This effect can be accredited to templating of the SiNPs to functional groups present on the cell wall. Additionally, the ink preparation method may attribute to a change in mixture composition. In preparing the ink with added biocatalysts, pH adjusted SiNPs were first mixed with PAM and then the PBS. The biocatalysts were then resuspended by this mixture and added to a given amount of glycerol. Therefore, with the addition of biocatalysts to the first mixture of SiNPs, PAM, and PBS, the transfer volume via pipette would stay constant, thereby decreasing the overall transfer amount of SiNPs, PAM, and PBS as the biocatalysts would contribute some volume. With the lower total volume of SiNPs, the ratio of TEOS:SiNPs would increase, leading to more cross-linker per volume SiNPs, causing the faster gelation kinetics.

After the gelation time was characterized, the mechanical properties of the gel, including the compressive modulus and the yield strength, were measured. Again, two trials were conducted: one with varied PAM wt% when mixed with the SiNP colloidal suspension (cell loading density constant at 0.00 g/ml), and one with varied cell loading

density (using GFP expressing *E. coli* and holding PAM wt% to 2wt%). 5 cylindrical samples of each test specification, measuring 8 × 5 mm (diameter × height), were prepared in silicone molds with TEOS contributing 11.5% of the total volume as would contribute to the final printed and processed silica gel. Molded samples were used for this experiment in order to investigate the intrinsic mechanical properties of the developed gel. The samples were removed from the molds after 24 hours and introduced into a PBS bath to further age the samples without allowing the samples to dry. After the PBS bath, the samples were tested in a dynamic mechanical analyzer (TA Instruments) with an 8mm parallel plate geometry.

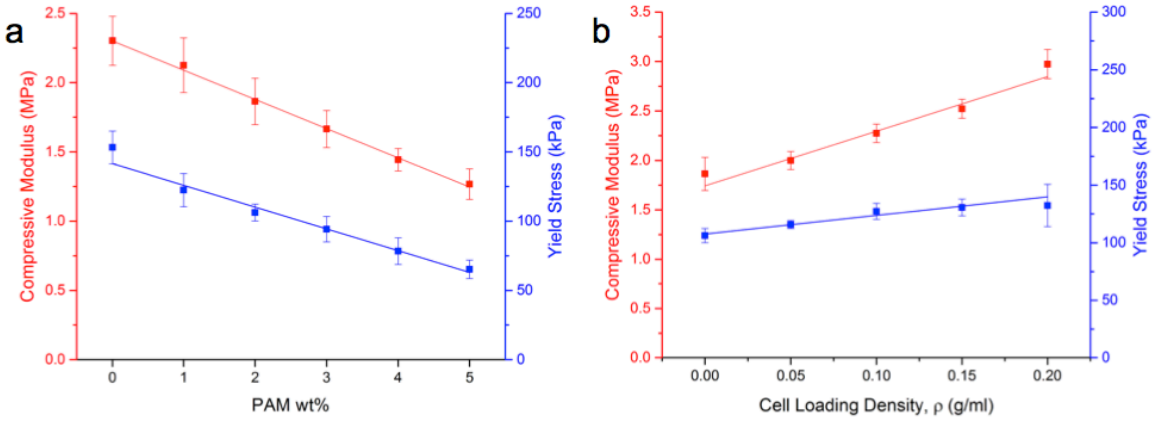

Figure 9. Mechanical properties characterization of varied gel compositions: compressive modulus and yield stress dependence on a) PAM wt% as mixed with SiNPs and b) cell loading density. Error bars represent standard deviation with n=5.

As the weight percent of PAM addition to SiNP suspension increased, both the compressive modulus and the yield strength were affected with a negative relation (Figure 9a). Decrease of the compressive modulus with an increase in PAM weight percentage allowed for higher strain within the bulk material at a given applied stress. This was important for 3D printing because of the ink-substrate interaction. As the ink was deposited from the printing nozzle, that filament contacted the substrate (glass slide

for first layer, and previous printed layers for all subsequent printed layers) and was elongated as the contacted portion adhered to the substrate while the printer nozzle moved. Without a decrease in the compressive modulus, it was observed that the silica-based ink was too brittle and would easily crack if the nozzle offset and printing speed were not fully optimized. Therefore, the decrease in modulus allowed for enhanced flexibility in the developed ink. An increase in PAM wt% gave a lower yield strength; this was a caution to not increase the PAM wt% to too high of value in order to ensure structural stability. Therefore, the PAM wt% was selected to be 2 wt% by weighing printability improvements with yield strength weaknesses.

As shown in Figure 9b, it was observed that as the cell loading density increased, the compressive modulus and yield strength increased. This can be explained through the gel preparation as described previously. With using the mixture of pH adjusted 2 wt% PAM SiNPs and PBS for re-suspension of the cells, the addition of the cells would decrease the overall volume of transferred SiNPs to be mixed with a prescribed volume of TEOS. Therefore, the ratio of TEOS:SiNPs increased, providing a higher cross-linker to base ratio, which would increase gel strength. This would cause the gel to strain to a lower magnitude for a given stress as compared to samples with a lower cell loading density. Similarly, with a higher cross-linker to base ratio, the gel would increase in overall strength, shown through the increase in yield strength.

Another critical aspect for the use of biocatalysts within a 3D printed ink was the bacterial distribution within the gel. To provide a quantitative assay of the distribution of the cells within the gel, a χ^2 probability test was utilized to identify the probability that

one can confidently accept the null hypothesis of a homogenous distribution of biocatalysts. 3 circle samples were printed, with $\rho = 0.05$ g/ml of *E. coli* tagged with green fluorescent protein (GFP), and the distribution was mapped via the use of confocal microscopy (Figure 17a,b). $\rho = 0.05$ g/ml was used in order to clearly separate cells within the confocal mapping for higher accuracy in location of the encapsulated cells. The confocal microscope mapping was then counted and analyzed with the developed χ^2 MATLAB code (Appendix A) to determine the probability that the distribution was uniform. Across 4 locations in each of the three samples, the calculated P-value attained was 0.999 with an uncertainty of 0.001 providing extremely high confidence in homogeneity of the biocatalyst distribution within the ink.

3.4 Batch Reactor Experiment

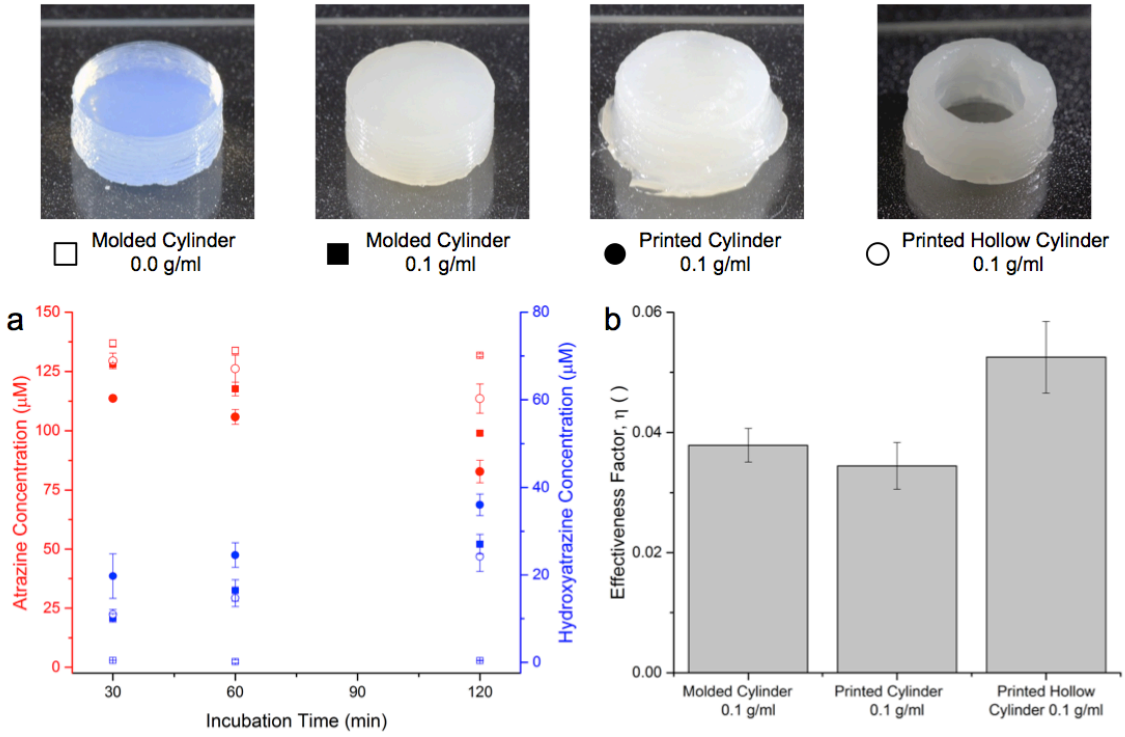

Figure 10. Batch reactor biodegradation experiment: a) atrazine and hydroxyatrazine concentrations from each sample type at different incubation lengths and b) effectiveness factor comparison given by the ratio of the observed reaction rate in the gel over the previously presented maximum observable reaction rate (molded cylinder with no bacterial loading was omitted due to no degradation). Tests were completed in triplicate.

After the printing process was developed, the bioremediation capability of printed biocatalysts was tested in batch reactor experiments. Four sample types were tested, consisting of molded cylinders 1) without biocatalyst loading and 2) with 0.10 g/ml AtzA biocatalysts along with printed 3) cylinders and 4) hollow cylinders, both with 0.10 g/ml AtzA biocatalyst loading. The sample types are given in Figure 10. Sample types 1 and 2 were molded for two hours within silicone molds to obtain cylinders measuring 10 × 5 mm (diameter × height). Printed cylinders were designed to be analogous to the molded cylinders in dimensions and the hollow cylinders were printed to a wall thickness of 2

mm, inner diameter of 8 mm, and height of 5 mm. Each sample type was introduced to a test vial with 5 ml of 150 μM atrazine and placed on a microplate shaker at 130 rpm for the prescribed batch length (30, 60, and 120 minutes). Atrazine and hydroxyatrazine concentrations were measured via high performance liquid chromatography (HPLC) analysis for each sample type in triplicate.

Through the batch reactor experiments, it was confirmed that the AtzA biocatalysts sustained the ability to biotransform atrazine to hydroxyatrazine when encapsulated in the developed silica hydrogel and when 3D printed (Figure 10a). In comparison between the control samples of the molded cylinders with $\rho = 0.00$ g/ml with the molded cylinders with $\rho = 0.10$ g/ml, the incorporation of the biocatalysts allowed for biotransformation of atrazine to hydroxyatrazine. The sustained decrease in atrazine concentration by the control samples were attributed to absorption of the atrazine into the silica gel. Further decrease in atrazine concentration attained by the molded cylinders with $\rho = 0.10$ g/ml was due to bioremediation of atrazine by the AtzA biocatalyst, proven by the rise in concentration of hydroxyatrazine over time. Validation of the ability of biocatalysts within 3D printed samples was also shown as the atrazine concentration decreased, with hydroxyatrazine concentrations increased.

In comparing overall reaction rate of the biotransformation of atrazine to hydroxyatrazine between the sample types, the effectiveness factor, η, was calculated. The effectiveness factor is a dimensionless factor that gives the ratio of the observed reaction rate within the silica gel, r_{obs}, to the maximum observable reaction rate without diffusional limitations, r_{max}.[69] Both reaction rates are given by units of μmol/min/g-cell. It

was assumed that r_{max} was equal to previously reported free cell biotransformation of atrazine.[70] The effectiveness factor was calculated through the slope of hydroxyatrazine production over time divided by the average cell loading mass.

As shown in Figure 10b, the effectiveness factor increased between the printed cylinder with a biocatalyst loading of 0.1 g/ml and the printed hollow cylinder with a biocatalyst loading of 0.1 g/ml. This can be explained by a decrease in atrazine concentration decreasing overall biocatalyst usage as cells located closer to a surface would degrade all incoming atrazine, leaving no atrazine for internally located cells to degrade. Additionally, as the concentration gradient between the atrazine solution and the silica gel decreases, less diffusion of atrazine into the gel would be observed, decreasing overall biotransformation. It was observed in comparing the printed hollow cylinders to printed cylinder, that as the SA:V ratio was increased, the reaction rate was sustained further into the test. Therefore, the application of bioremediation with 3D printing capabilities allows for improved cell usage as structures may be developed to decrease diffusional limitations via an increased SA:V ratio.

3.5 Flow-Through Reactor Experiment

With verification of bioremediation capability within 3D printed structures with silica-encapsulated biocatalysts, capacity of this technology to flow-through reactor design was investigated through both simulation and experimentation.

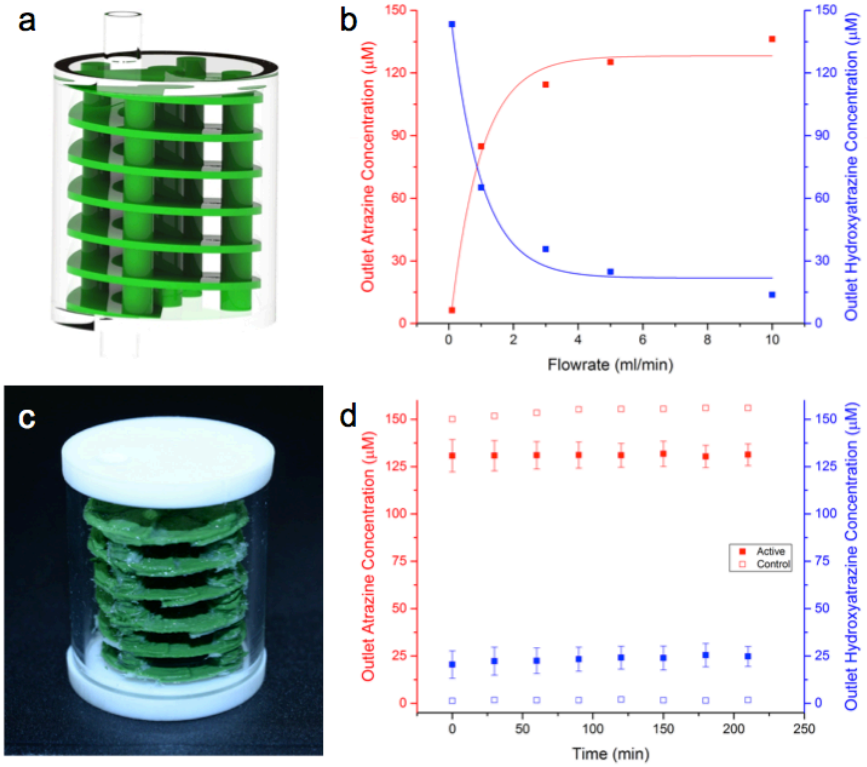

Figure 11. Flow-through bioreactor simulation and experimental results: a) 3D CAD design of flow-through bioreactor to be implemented into ANSYS for b) produced steady-state simulation results from an inlet concentration of 150 μM at various flowrates. c) Flow-through reactor fabricated from 3D printed spiral (green) and capsule for d) experimental degradation of atrazine tested at various time lengths. Experimental results produced in triplicate.

First, the computer aided design (CAD) model of the flow-through reactor was designed to incorporate high SA:V ratio characteristics along with flow directing features to improve residence time of the atrazine solution within the reactor (Figure 11a).

Reaction-flow simulations were completed via ANSYS CFX. The reaction rate for free AtzA biocatalysts was identified in previous publications and applied within the spiral portion of the simulation, identified as the silica domain.[70] Additional inputs to the model were the gel porosity and the diffusion coefficient of atrazine through the developed gel. These inputs were found through experimentation. The gel porosity, ϕ,

was calculated as $\phi = 0.804 \pm 0.009$. The diffusion coefficient was calculated to be $D_{eff} = 2.2 \times 10^{-3} \frac{\text{mm}^2}{\text{s}}$.

Simulations were completed for inlet flowrates of 0.1, 1, 3, 5, and 10 ml/min. The outlet concentrations of atrazine and hydroxyatrazine were given in Figure 11b. As the inlet flowrate increased, the residence time of the atrazine within the device decreased, leading to less degradation denoted by higher outlet concentrations of atrazine and lower outlet concentrations of hydroxyatrazine. Addition details on the simulation were given in the following chapter (Figure 21).

From the modeling, it was important to identify flowrates that would be attainable in experimental practice and that would yield measurable results. Because of this, the flowrate of 1 ml/min was selected as this showed promise in the significant degradation of atrazine. Analogous spirals with silica-encapsulated AtzA biocatalysts were 3D printed by the previously described method and the flow-through bioreactor was fabricated with a glass tube and Teflon caps (Figure 11c). The flow-through experiment (Figure 22) was completed with an inlet flowrate of 1 ml/min and consistent degradation was proven through 30 min measurement intervals of the outlet solution. Atrazine degradation was consistent at an average outlet concentration of 131 ± 7 μM across the measured time points, equating to a degradation percent of 15 ± 5% of the inlet atrazine. Hydroxyatrazine was produced at an average outlet concentration of 23 ± 6 μM (16 ± 4% of inlet atrazine biotransformed). The discrepancy between the outlet concentrations not summing to 150 μM can be attributed to the error intrinsic to the HPLC analysis (5% error).

Overall, the 65% difference between the simulation and experimental results may be associated with numerous factors. First, the fabricated flow-through bioreactor was not fully accurate to the model input to the simulation. As the silica 3D printed spiral needed to be inserted into the glass tube, there was a gap between the print and the glass wall. This allowed a small portion of the flow to bypass the spiral, which would lead to decreased degradation within the experiment as compared to the simulation. Secondly, the reaction rate may be hindered in the experimental setting as some biocatalysts would be non-functional within the 3D printed structure, this resulting from denaturation during either the encapsulation or printing processes.

3.6 Project Conclusions

Atrazine, a near ubiquitous herbicide in the United States, represents a large-scale environmental problem through its heavy use and easy dispersal leading to health and environmental issues. Through the material flexibility, precision in spatial deposition, and application specific geometry design, direct-write 3D printing has been presented as a viable option for removal of atrazine from the environment through a developed flow-through bioreactor design. The novel 3D printing process incorporated a silica-based hydrogel produced via the sol-gel method with encapsulated biocatalysts that were shown to perform active bioremediation of atrazine within both batch reactor and flow-through reactor experiments. Geometries with high SA:V improved degradation efficiency. Additionally, flow-through bioremediation was simulated and compared to the experimental results.

In order to apply the presented work to other fields, one would simply design the printed materials with two factors in mind: the specific microorganism to conduct the desired biotransformation and the 3D printed geometry that would optimize the process for the given application.

From this work, we have opened the gate of utilizing 3D printing in applied microbiological technologies for bioremediation purposes. Further work may produce structures with numerous bacterial strains to overcome other grand issues present in the environment through multistep degradation pathways that transverse multiple biocatalysts. With 3D printing, the overall geometry may be optimized to enhance the transport of degradation products from one biocatalysts population to another through spatial control of multi-material printing containing the different bacterial strains. This printing of sol-gel materials with encapsulated microorganisms can be expanded to produce significant advances in the fields of environmental, pharmaceutical, medical, and material sciences.

CHAPTER 4

Additional Project Details

4.1 Bacterial Strains and Growth Conditions

Two bacterial strains were utilized in the presented project: *E. coli* DH5α (pMD4) and *E. coli* K12 MG1655 (pUA66-GFP).[55,71] Both strains were grown at 37 °C in Luria–Bertani (LB) while shaking at 240 rpm. During shaking, the strains were supplemented with 30 μg mL-1chloramphenicol (E. coli DH5α (pMD4)) and 50 μg mL-1 kanamycin (E. coli K12 MG1655 (pUA66-GFP)). Starter cultures were produced through inoculation of LB media with cells from a single colony. The starter cultures were then grown until they reached stationary phase and cell production flasks were inoculated with 10 % (v/v) of the stationary-phase cultures. Finally, produced cells were harvested by centrifugation at 6,000 rpm for 10 min at 4 °C.

4.2 High-Resolution Printing of Silica Sol-Gel Ink

With the developed 3D printer ink, we showed further ability to control the deposition of the ink in Figure 12. Here, we printed through an 80 μm (inner diameter), or 33 gauge, printing nozzle, the Block M of the University of Minnesota. This structure demonstrated the controlled deposition of the ink through sharp features requiring 1) adhesion between the printing substrate (microscope glass slide) and the printer ink, 2) optimized offset distance (distance between printing substrate and extrusion nozzle) and printing speed (velocity that the extrusion nozzle translates in plane parallel to the

printing substrate), and 3) controlled and consistent deposition of the ink to provide a constant printed structure without discontinuities. Overall printing time was < 10 s.

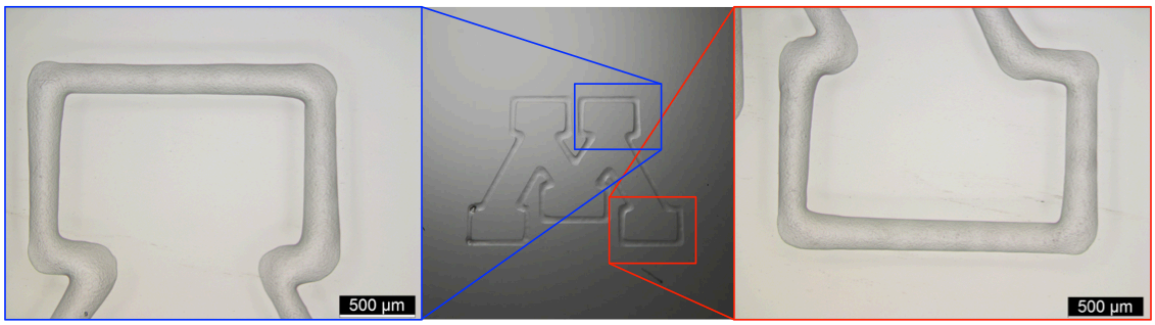

Figure 12. Printing of silica based 3D printer ink showing high-resolution printing. Ink composition was a ratio of 78.57 : 3.93 : 15.00 : 2.50 (SiNP : TEOS : Glycerol : PBS). Printing was completed with an 80 µm (inner diameter) printing tip, extrusion pressure of 150 kPa. The ink was not loaded with bacteria for simplicity. Left and right images taken on optical microscope (10x magnification). Central image was taken with a DSLR camera (micro-lens).

4.3 Detailed Methods for Ink Mechanical Properties

Numerous mechanical properties were measured in order to fully understand the gel and how the gel will interact with its environment in further experiments.

The gelation time was measured in order to understand the effect of PAM and bacterial loading on the sol-gel transition rate. It was observed that with varied amounts of each PAM and bacterial loading, the mixture would transition to a gel in different time scales. This was necessary to investigate due to the need to readily prepare ink at appropriate times so as to minimize overall printing time by decreasing ink change over times.

Compression testing was run on molded cylindrical specimens in order to investigate elasticity and yield points of the material when under mechanical stress. This was necessary to determine the effect of PAM content and bacterial loading on the elasticity and yield point of the overall gel.

4.3.1 Gelation Time Experimental Methods

In conducting the gelation time measurements, the AR-G2 Rotational Rheometer (TA Instruments) was run in the time-sweep procedure. This procedure called for the top parallel plate of the rheometer to be rotated at various frequencies, and at each frequency, the value of *tan(δ)* was measured. This is in accordance with previously published methods by Ponton et al.[66] The value of *tan(δ)* is given by *G''/G'* (loss modulus/storage modulus). Since the loss and storage moduli describe viscous and elastic properties, respectively, this method utilizes the frequency dependence of *G''/G'* to determine gelation point. As a non-gelled fluid is tested, the top plate rotates at three frequencies – 0.50, 1.75, and 3.00 Hz. Because a fluid reacts elastically when influenced by an instantaneous force (characterized by a high frequency movement) and fluidly when experiencing a steady force over a longer time period (characterized by a low frequency movement), the value of *tan(δ)* is frequency dependent until $t=T_{Gel,}$ the gelation time. Therefore, the lower frequencies will start the test when the sample is still fluid with higher values of *tan(δ)*, crossing the lower values given by the 3.00 and 1.75 Hz data as the fluid transitions to a solid. The point at which the low frequency data crosses the high frequency data determines the time of gelation, as depicted in Figure 13, below.

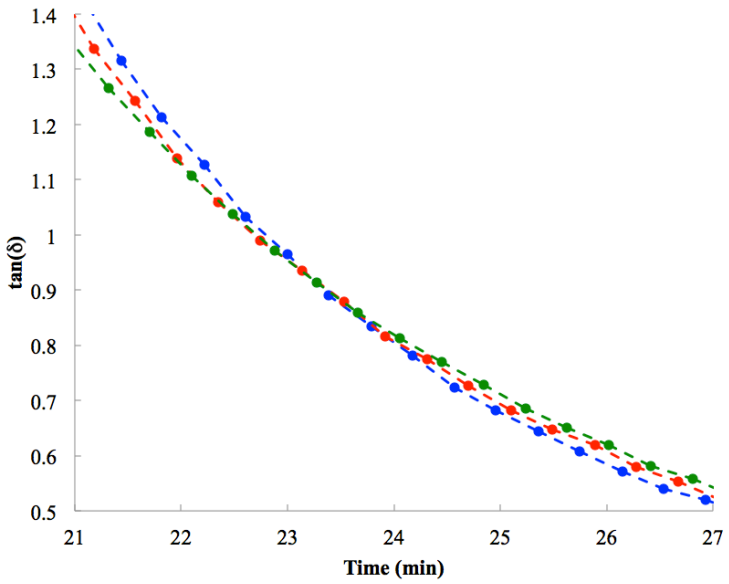

Figure 13. Example gelation time data analysis. Determination of time of gelation, T_{Gel}, from parallel plate rheological methods. Blue, red, and green data series represent 0.50, 1.75, and 3.00 Hz series, respectively.

In the above Figure 13, T_{Gel} may be measured to be 23.3 minutes as this is the point where the three frequency series data cross as the material gels.

Rotational rheology was used to measure the gelation time of the silica based 3D printer ink. The tests were completed within the Polymer Characterization Facility (Department of Chemical Engineering and Materials Science, University of Minnesota), utilizing the AR-G2 Magnetic Bearing Rheometer (TA Instruments) with a parallel plate geometry. The setup within the AR-G2 is described by Figure 14, given below.

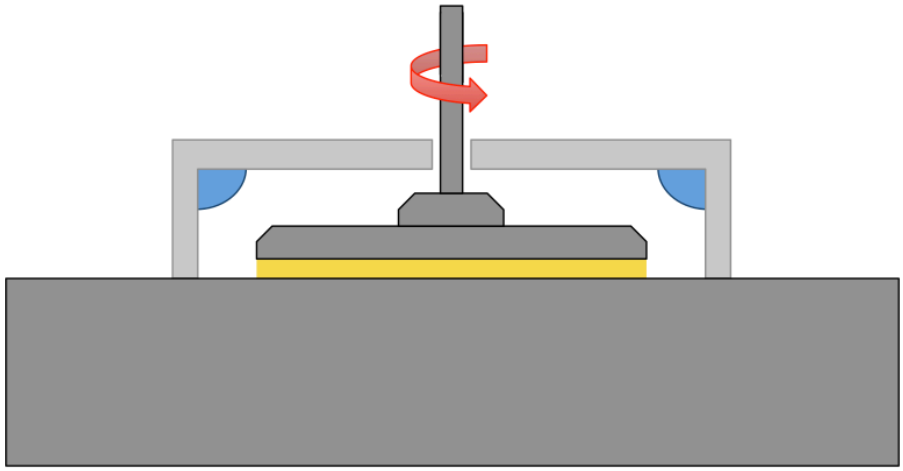

Figure 14. Setup for gelation time testing on the AR-G2 Magnetic Bearing Rheometer.

As shown in Figure 14, the sample (yellow) was pressed between two parallel plates that included a 40 mm circular flat plate geometry and a 80 mm Peltier heating base. To decrease the chance of sample drying due to environmental dehumidification effects, a humidification barrier (light grey), with KimWipes soaked with distilled water (blue), was placed around the sample during testing. Within the bottom plate, the Peltier heating element was utilized to ensure consistent temperature control over the current test sample.

Samples were prepared by mixing the SiNPs with PAM and PBS, with or without resuspended *E. coli* expressing GFP, and glycerol. Generally, Ludox HS-40 colloidal silica was mixed with the PAM (to the target wt% value, 2 wt% PAM for all variable cell loading samples) via magnetic stir bar for 2 hours in a 20 ml scintillation vial. In another 20 ml scintillation vial, the bacteria were transported from the 50 ml centrifuge tube that the bacteria were collected in during centrifugal compaction to form a cell pellet. The 20 ml scintillation vial was placed on a scale, the scale was zeroed, and the cells were transferred to the scintillation vial until the desired amount was reached. The bacteria

were then resuspended from the pelletized state by vortex mixer with PBS. The SiNP-PAM solution was then pH adjusted with HCl in a 10:1 ratio (SiNP-PAM:HCl). This pH-adjusted solution was then mixed with the resuspended bacterial solution to the desired ratio (vortex mix).

The mixtures without cross-linker were then transported to the polymer characterization facility in scintillation vials where the testing apparatus was setup and calibrated as defined by the AR-G2 superuser, user interface initialized, and environmental conditions set (Peltier plate set to 22 °C). The cross-linker was then added and the mixture stirred by hand with a plastic spatula for 25 seconds to ensure adequate homogeneity of the developed material. Overall, the volumetric makeup of the gel in percent was 78.57 : 3.93 : 15.00 : 2.50% (SiNP-PAM : TEOS : Glycerol : PBS). The sample was then transferred from the scintillation vial to the parallel plate geometry via a 1 ml syringe (0.60 ml of material transferred). The gap between the parallel plate geometry was then adjusted to 500 μm, and the humidification barrier was placed.

The testing program was started when the target gap was attained, and the time from TEOS addition to first data point was measured via stopwatch, and recorded for later data manipulation. The testing procedure included the top plate oscillating at 0.50, 1.75, and 3.00 Hz to a strain percentage of 5%. Data sets were taken every 24 s, with each data point requiring 8 s of oscillation prior to recording data for each frequency. Only 3 testing frequencies were used due to the delay in data collection that additional testing frequencies would add. Samples were run until the gelation point was observed through the *tan(δ)* vs. *time* plot on the user interface of the equipment software.

4.3.2 Compression Testing Experimental Methods

In testing the developed material in compression, we aimed to investigate the intrinsic strength and elasticity of the material. To do this, we first determined the compressive moduli by calculating the slope of the initial linear portion after uneven face effects had passed. With an increase in slope, the compressive modulus increased, providing that the material would strain less for a given applied stress. As the slope lessened, the compressive modulus decreased, leading to a material response that would allow for higher strain under the same applied load. It was of interest to test PAM wt% addition to the SiNP solution to investigate the elastic response of a material impregnated with long-chain polymers when applied with a load. Additionally, the yield point of the material was investigated to identify weakening of the structure due to polymer and bacterial addition. These variables were seen as templating and point defect additions, respectively, and to identify the true effects on material response, these were necessary tests. Typical collected data is represented by Figure 15, given below.

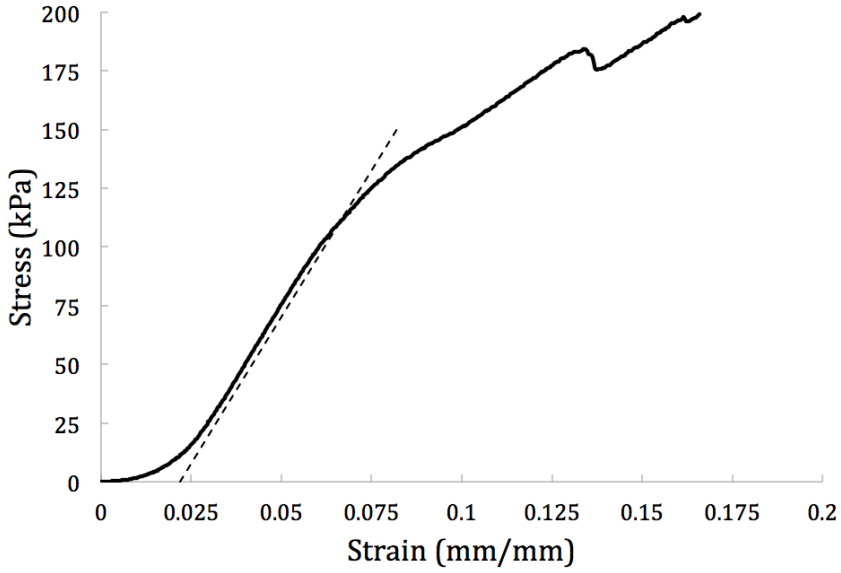

Figure 15. Example stress vs. strain data analysis for a cylindrical specimen of developed silica-based ink materials. Test data given by solid line data series and 0.2% strain offset given by dotted line data series.

To determine the compressive modulus, the linear portion found after the initial non-flat face effects (curved portion from 0-0.03 strain in the above example data analysis) was analyzed. The slope of this was taken as the compressive modulus and the yield point was attained by an offset of 0.2% strain with the same slope.[72] The point of intersection between the offset and data gives the yield stress of the material.

DMA rheology was utilized to measure compressive moduli and yield points of the developed 3D printer ink material with added TEOS for structural enhancements. These tests were also completed in the Polymer Characterization Facility (Department of Chemical Engineering and Materials Science, University of Minnesota), on the RSA-G2 Solids Analyzer (TA Instruments), with 8 mm circular compression plates. Below in Figure 16, the experimental setup is depicted.

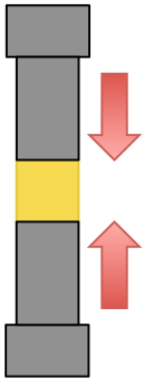

Figure 16. Setup for compression testing on the RSA-G2 Solids Analyzer.

As shown in the diagram above, the cylindrical sample (yellow) was compressed between two 8 mm circular plates (grey), at constant displacement rate.

For 3D printing, it was deemed necessary to post process the silica-based 3D printer ink through addition of cross-linker to counteract sagging of printed structures. In order to incorporate the effect of this post processing, molded cylinders with an equivalent amount of cross-linker (TEOS) were produced. First, silicone molds were 3D printed using the Aerotech A3200 on standard 75 x 25 mm glass microscope slides. The molds measured 8 x 5 mm (inner diameter x height). The molds were stored in atmospheric conditions for 24 hours to allow solvent evaporation. After 24 hours, the gel was prepared. Similar to the gelation time samples, the gel was prepared in 20 ml scintillation vials. The Ludox HS-40 colloidal silica was mixed for 2 hours with the target wt% of PAM on a stir plate. The bacteria were transferred to another 20 ml scintillation vial and resuspended with PBS via a vortex mixer. The SiNP-PAM solution was pH adjusted (10:1 with HCl) and mixed with the resuspended bacteria. Glycerol was added and the mixture was vortex mixed to promote homogeneous distribution of bacteria within the liquid. The liquid was then placed on a stir plate with a small stir bar within

the scintillation vial. The TEOS cross-linker material added and the stir bar was used to mix the solution for 10 seconds. After 10 seconds, the mixture was transferred from the scintillation vial to the mold via a 1 ml syringe (0.3 ml of mixture for each mold). Once the mixture was introduced into the mold, a siliconized cover slide was placed on top of the mold to ensure flat contact surfaces of the cylindrical samples for improved compression testing. The volumetric makeup of the gel in percent was 72.40 : 11.50 : 13.80 : 2.30 (SiNP-PAM : TEOS : Glycerol : PBS). After 24 hours within the mold, the siliconized cover slide was removed carefully and the silicone mold was cut away from the cylindrical sample. The sample was then placed in a PBS bath for 24 hours prior to testing.

The samples were transported to the Polymer Characterization Facility (University of Minnesota) within the PBS bath and only removed from the bath immediately before compression testing. Excess surface water was removed and the samples were measured for diameter and height by linear caliper. After ensuring the sample was without defects and dimensionally accurate, the sample was placed within the test fixture within the RSA-G2.

The round plate geometry was utilized for compression testing at a constant velocity. The test was run until strain reached 30%, where this value ensured that all the necessary data was recorded for analysis of both the compressive modulus and the compressive yield point.

4.4 Characterization of Bacterial Loading within 3D Printed Silica Sol-Gel

4.4.1 Characterization of Bacterial Distribution

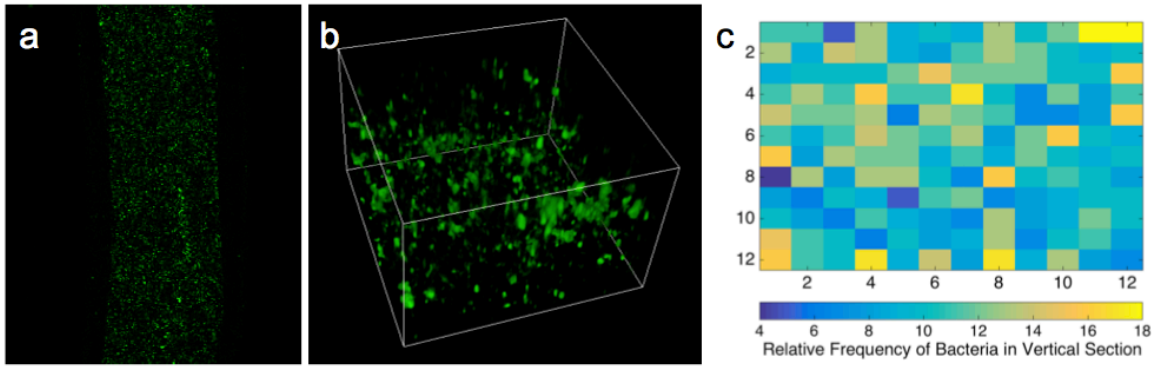

Figure 17. Confocal microscopy of cell distribution in 3D printed circular structures: a) 2D fluorescent image of bacterial distribution and b) 3D confocal mapping of microbial distribution. c) MATLAB c^2 analysis for quantification of the distribution homogeneity.

To further characterize the printed ink properties, the cell distribution within the 3D printed ink was measured through confocal imagery of GFP expressing *E. coli.* 3 circle samples were printed through a 200 μm printing nozzle at 100 kPa. The Nikon A1 rsi Confocal Microscope was used to excite and image the GFP within each encapsulated bacteria. Lasers with emission peak wavelength of 488 nm were used to excite the GFP, which produced emitted light at 510 nm. Through the use of filter cubes, the light that was imaged only contained that of the emitted so as to not bleach the images with overlighting. Samples were protected from drying while under the excitation laser through applied PBS droplets.

4.4.2 Live / Dead Assay of 3D Printed Bacteria

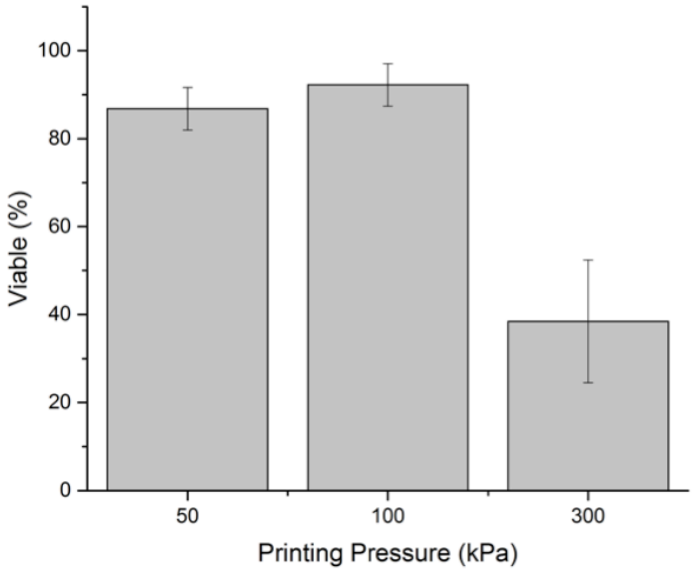

Figure 18. Viability assay of 3D printed biocatalysts extruded at various printing pressures. n=3 for all printing pressures.

Additionally, cell viability through the printing process was investigated (Figure 18). *E. coli* expressing the AtzA enzyme were encapsulated in the developed 3D printer ink at ρ = 0.05 g/ml and simple single-layer circle structures were printed at 50, 100, and 300 kPa. After printing, a bacterial viability assay (ThermoFisher Scientific) was used to quantify the numbers of cells that were alive and dead (compromised cell membrane). This assay was comprised of both SYTO® 9 nucleic acid stain and propidium iodide. SYTO® 9 works as a cell membrane permeant, a molecule that is able to pass through the cell membrane naturally, and binds to the DNA of the cell, where it will emit green light (503 nm) when excited by 488 nm blue-green light. Propidium iodide on the other hand labels cells with compromised cell membranes. As a cell membrane is compromised, the propidium iodide molecules are able to infiltrate the cell, where it will then bind to the DNA and emit red light (636 nm) when excited by green light (493 nm). Therefore, all

cells will be labeled with the green emitting SYTO® 9 dye, but when the membrane is compromised, the propidium iodide enters and emits red light within that cell as well as the already emitting green light.

To stain the printed structures, concentrated stain solutions were formulated from 1 ml PBS and 10 μL of each dye. The stain solution was then administered to the printed structures for 30 minutes to allow diffusion of the dye throughout the printed structures. After 30 minutes, the dye was removed and the structure was washed with PBS.

The Nikon A1 rsi was used to image the structures and the images were then analyzed through counting of the cells showing on the propidium iodide and the SYTO® 9 channels. The number of alive cells were taken as the difference between the number showing on the SYTO® 9 channel and the number counted on the propidium iodide channel since those that are dead would emit both green and red light. The dead cells were taken as the number counted only on the propidium iodide channel.

From the results, it was clear that cell viability dropped significantly between printed samples at 100 kPa and 300 kPa.

4.5 Additional Gel Characterization for ANSYS Simulation Input

4.5.1 Atrazine Diffusivity within Developed Silica Ink

Another mechanical aspect of the developed silica hydrogel 3D printer ink that was important to understand was the diffusivity of atrazine through the gel. This characteristic of the gel was measured to ensure that the developed gel did not function to transport atrazine at a rate much lower than previously reported values by Mutlu et al.[70]

With attaining a value for the diffusivity constant near that which Mutlu reported $\left(D_{eff} = 3.51 \times 10^{-4} \frac{\text{mm}^2}{s}\right)$, we can ensure that the diffusion of the atrazine through the gel would not hinder the degradation process to a great extent. In addition, this value was utilized in computational models for accurate simulation of the overall flow-through degradation of atrazine. In order to calculate the diffusivity constant, *D*, Fick's First Law was used, as given in Equation 1, below.[73]

$$F = D\frac{dC}{dx} \tag{1}$$

Where *F* is the flux of the transported species $\left(\frac{\text{mol}}{\text{m}^2\text{s}}\right)$, *D* is the diffusion coefficient $\left(\frac{\text{mm}^2}{\text{s}}\right)$, *C* is the concentration gradient $\left(\frac{\text{mol}}{\text{L}}\right)$, and *x* is the length of diffusion, or barrier thickness (m). Therefore, in our experiment, we aimed to control the concentration gradient, *C*, and the barrier thickness, *x*, while measuring the flux of atrazine, *F,* in order to calculate *D,* the diffusion coefficient of atrazine through our developed 3D printer silica gel ink.

In order to measure the diffusivity constant, the following testing apparatus, given in Figure 19, was utilized.

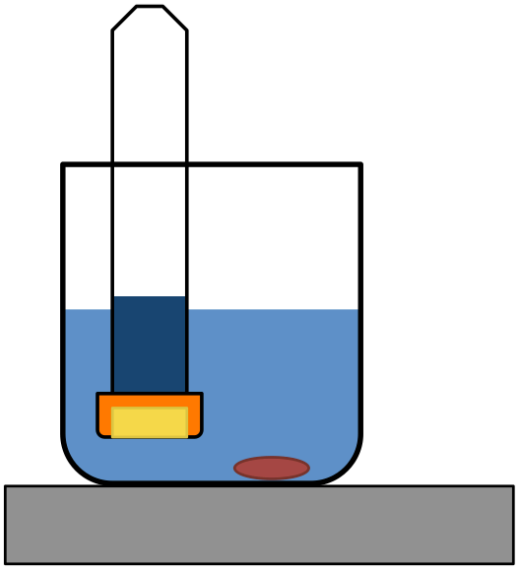

Figure 19. Experimental setup for measurement of atrazine diffusivity.

In the above figure, the grey box represents the stir plate used to control stir bar (red) for adequate mixing within the beaker (black outline). 5 ml of phosphate buffer (PB) was added to each test setup (light blue). A 15 ml centrifuge tube was used to house the gel test sample (yellow) and the centrifuge tube contained the 150 μM atrazine in PB solution (dark blue). The centrifuge tube was held in a position 1-2 mm above the bottom of the beaker and on the other side of the beaker so that the stir bar would not contact the test gel, causing damage to the sample.

Prior to gel preparation, similarly to the compression samples, the mold needed to be prepared so that the silica gel could be transferred to the mold prior to gelation. In this instance, the mold was formed from the 15 ml centrifuge tube cap.

To house the silica gel, a 1 cm diameter hole was punched from the cap of the 15 ml centrifuge via a 10 mm bone biopsy punch. The exterior of the cap was then covered with Parafilm to form the interface side of the gel between the gel and the PB. The inside of the cap contained a seal that was used as a retaining wall so that a the silica gel could

be poured into the cap to produce a 10 mm diameter, 3.65 mm tall cylindrical sample for diffusion testing. Once the hole was punched and the Parafilm applied, the gel was prepared.

2% wt. PAM silica gel samples were prepared similarly to that given in section 4.3.2. The SiNP-PAM mixture was introduced to the glycerol and mixed thoroughly via vortex mixer. After homogeneity was reached, the cross-linker was introduced to conform to the 72.40 : 11.50 : 13.80 : 2.30 (SiNP-PAM : TEOS : Glycerol : PBS) volumetric makeup for molded specimens. This was completed within a 20 ml scintillation vial with a small stir bar, on the stir plate. Therefore, adequate mixing of the cross-linker with the base materials was attained quickly with an active stir bar as the cross-linker was introduced. After 10 seconds of mixing, 350 μL of the solution was transported to the 15 ml centrifuge tube cap mold via a 1 ml syringe. After introduction of the liquid solution to the mold, the samples were allowed to gel and age for 24 hrs.

After 24hrs, the Parafilm was removed and the 15 ml centrifuge tube cap was introduced to the tube portion with 5 ml of 150 μM atrazine in PB within the tube. The centrifuge tube was then rotated so that the cap with silica gel was facing the ground. The upper portion of the centrifuge tube was clamped by a ring stand and clamp system so that the silica gel was held 1-2 mm from the bottom of the beaker. The stir plate was used to control the stir bar to a constant 125 rpm throughout the experiment. 3 samples each were run for 2, 4, 6, and 8 hours. The concentration within the beaker at each time point was then measured via HPLC using a C18 column.

In order to accurately characterize the diffusivity of atrazine through the developed gel, the concentration within each sample was measured over multiple time points, and the calculated diffusion coefficient was found by averaging all samples together. The measured moles of diffused atrazine are given below in Figure 20 for all tested time points.

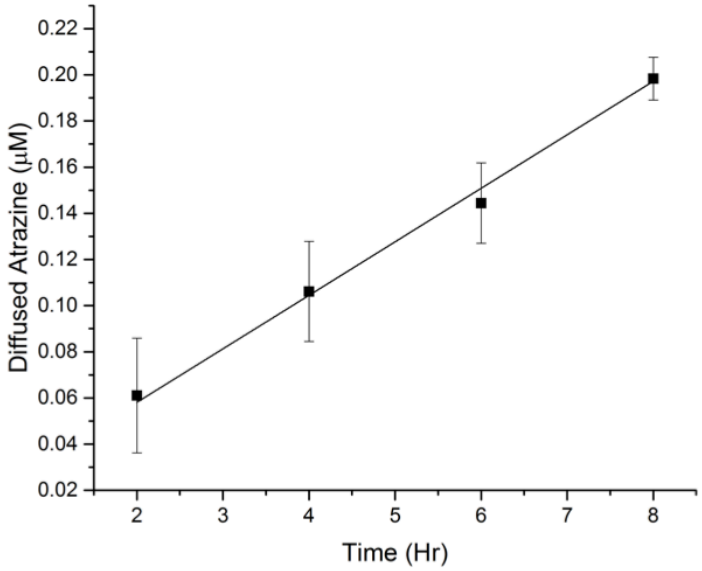

Figure 20. Experimental measurements of diffused atrazine per time length for characterization of diffusion coefficient. n=3 for all time points.

The outcome from this characterization yielded a diffusion coefficient, $D_{eff} = 2.2 \times 10^{-3} \frac{\text{mm}^2}{\text{s}}$. This value provides a diffusion coefficient over 6 times higher than the previously reported value for SiNP-TEOS gels. With the higher diffusion coefficient, we allow confidence in that our developed gel would not hinder diffusion of atrazine through the gel to lower the overall degradation rate. This value was used later in the ANSYS simulation of the flow-through bioreactor as an input for the diffusion through a porous material domain.

4.5.2 Silica 3D Printer Ink Porosity

In addition to the diffusion coefficient of atrazine through the porous domain input to the ANSYS biodegradation simulation, the program called for the porosity of the porous silica matrix. This was necessary to determine void space within the overall structure and accurately model the domain and atrazine transport through the domain.

Percent porosity, ϕ, is defined as the fraction of void space volume over the total volume as defined in Equation 2, below.[74]

$$\phi = \frac{V_{Void}}{V_{Bulk}} \tag{2}$$

Where V_{Void} is the volume of void space (mm^3) and V_{Bulk} is the overall volume of the produced gel structure. The difference in mass from before and after water content was removed from the gel allowed a calculated void volume. Manual linear measurements via caliper were used to calculate the bulk volume.

In order to improve the porosity measurements, larger cylindrical samples were produced to minimize measurement errors due to surface water. Larger samples helped for this due to a smaller surface area to volume ratio, providing that if the samples still contain some surface liquid, this would cause less of a deviation within the measurements. For the larger molds, 3D printed silicone molds were used where each two-part mold had 5 mold cavities, each measuring 12 mm in diameter and 11 mm in height.

To calculate the void volume, V_{Void}, PBS was used to saturate the gel that would later be driven from the gel to calculate the overall volume through a density relation with the mass of water removed. To remove the water content, the samples were placed

in a DX 302 Drying Oven (Yamato). In order to measure the mass of each sample before and after drying, a NewClassic MS Analytical Balance (Mettler Toledo) was used.

Two molds were used to produce 10 porosity samples. First, the gel was prepared analogously to that used in the compression samples testing. The SiNPs were mixed with 2 wt% PAM and then pH adjusted using 1 M HCl. The pH adjusted, SiNP-PAM mixture was then mixed with glycerol and then prepared on a mixing plate within a 20 ml scintillation vial. A small stir bar was added to the scintillation vial to mix thoroughly the mixture as the TEOS was added. The contents were added to form a volumetric percent ratio of 72.40 : 11.50 : 13.80 : 2.30 (SiNP-PAM : TEOS : Glycerol : PBS). After 10 seconds of mixing, the mixture was transferred to the silicone mold via pipette (~1.25 ml per cavity) and the lid of the mold was placed to mold accurate cylinders. The molds were left to complete the sol-gel process and age for 24 hours.

After 24 hours, each of the molded cylinders was removed from the silicone mold and measured with a caliper for diameter and height to be used to calculate the bulk volume. The cylinders were then placed within a PBS solution for 24 hours to fully saturate the gel. After 24 hours, the mass of each cylinder was measured using the analytical balance and recorded. Once the mass of the saturated cylinders were recorded, each sample was placed within a 20 ml scintillation vial (without cap) and placed within the drying oven for 24 hours. After the drying, the mass of each sample was again measured on the analytical scale and recorded. The porosity was then calculated as will be shown in the following section.

The 10 cylindrical samples were processed as given in the previous section and the both the bulk and void volumes were calculated. The void volume was calculated through using the density of water, $\rho_{H2O} = 9982 \frac{\text{g}}{\text{ml}}$ (neglecting the effect of retaining salts on the measured mass post evaporation of the water content from the hydrogel).[75] The bulk volume was calculated through the measured values of diameter and height for each cylinder.

Compiling these results and applying them to Equation 2, the resulting porosity, $\phi = 0.804 \pm 0.009$. This result describes a highly porous matrix that promotes water retention, allowing for high diffusivity of solutes as a high portion of the volume is occupied by water. The produced porosity result was later used as another input to the ANSYS simulation of the flow-through bioreactor.

4.6 ANSYS Simulation Details

The ANSYS model (Figure 21) was designed to incorporate the porosity, diffusion coefficient, and the reaction rate, as well as additional variables for the concentrations of atrazine and hydroxyatrazine. The transport of both atrazine and hydroxyatrazine were controlled by Equation 3, built into CFX.

$$\frac{dC_x}{dt} + \nabla \cdot (UC_x) = \nabla \cdot (D \nabla C_x) + S_{C_x} \tag{3}$$

Where C_x denotes the concentration of species x $\left(\frac{\text{mol}}{\text{m}^3}\right)$, U gives the velocity of the fluid $\left(\frac{\text{m}}{\text{s}}\right)$, D represents the diffusion coefficient of atrazine through the gel $\left(\frac{\text{m}^2}{\text{s}}\right)$, and S_{Cx} gives the source term controlling the rate of degradation of atrazine and production of

hydroxyatrazine $\left(\frac{\text{mol}}{\text{m}^3\text{s}}\right)$. Diffusion of atrazine was of prime importance, therefore, the diffusion coefficient of hydroxyatrazine was assumed to be the same as that for atrazine. Permeability of the silica gel was set to the lowest value possible within ANSYS, near zero at 1×10^{-20} m^2. This forced the diffusive transport to dominate within the silica domain, and fluid transport to dominate within the fluid domain. Turbulence was neglected within this model, as fluid flowrates through the device were low. Inlet concentration was held at 150 μM atrazine at variable flowrates across the different simulations. The outlet was held constant at a static pressure of 0 Pa. The degradation reaction was constrained to within the silica domain.

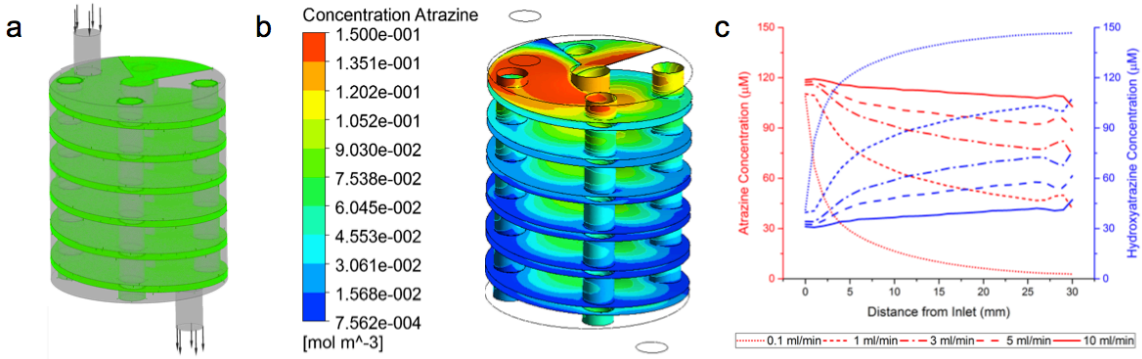

Figure 21. ANSYS simulation setup: a) boundary conditions for inlet and outlet of the domain and green highlighted reactive domain for atrazine degradation. Simulation results: b) mapping of 1ml/min atrazine concentration through reactive structure (note 1.500e-001 mol m^-3 is equal to 150μM) and c) Simulated results for various flow rates displaying average concentrations across planes perpendicular to inlet flow. Node count and element count for the developed simulation were 1,890,223 and 9,458,733, respectively.

4.7 3D Printed Flow-Through Bioreactor Experimental Setup

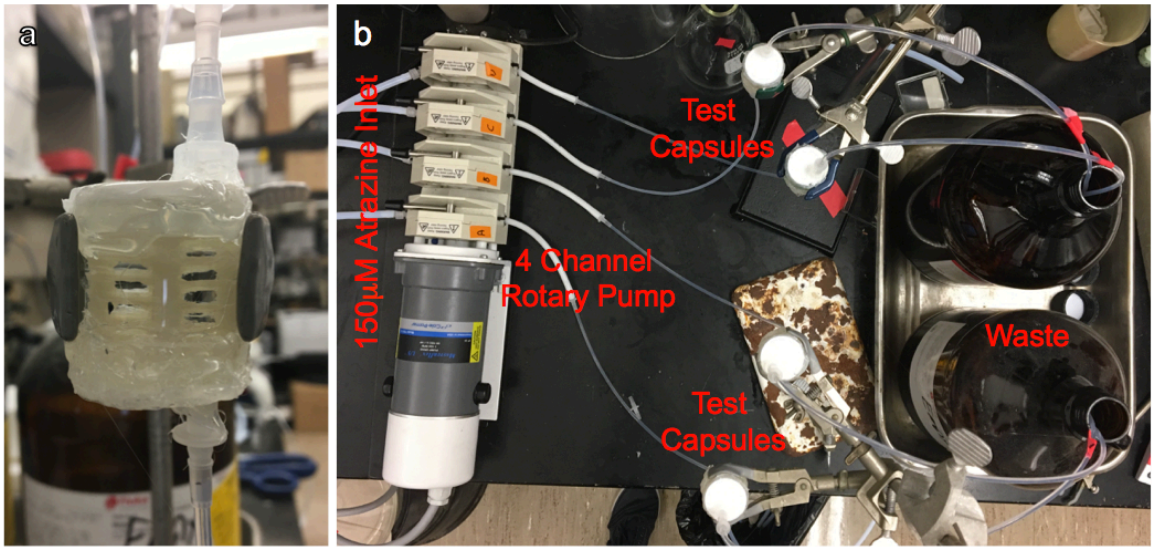

Figure 22. Flow-through bioreactor experimental setup: a) encapsulated 3D printed, biocatalyst loaded spiral placed inline as shown in b) experimental setup.

The flow-through experiment was completed on three samples printed with ρ = 0.1 g/ml of AtzA expressing *E. coli*, given in Figure 22a, and one control sample printed without cell loading. The flow was set to 1 ml/min using a 4-channel rotary pump from a 150 μM atrazine source. Teflon tubing was used so that no atrazine was adsorbed by the tubing, which would decrease the actual inlet concentration of atrazine. 1 ml samples were taken every 30 minutes to be analyzed through HPLC analysis to measure atrazine and hydroxyatrazine concentrations.

4.8 3D Printer Equipment & Setup

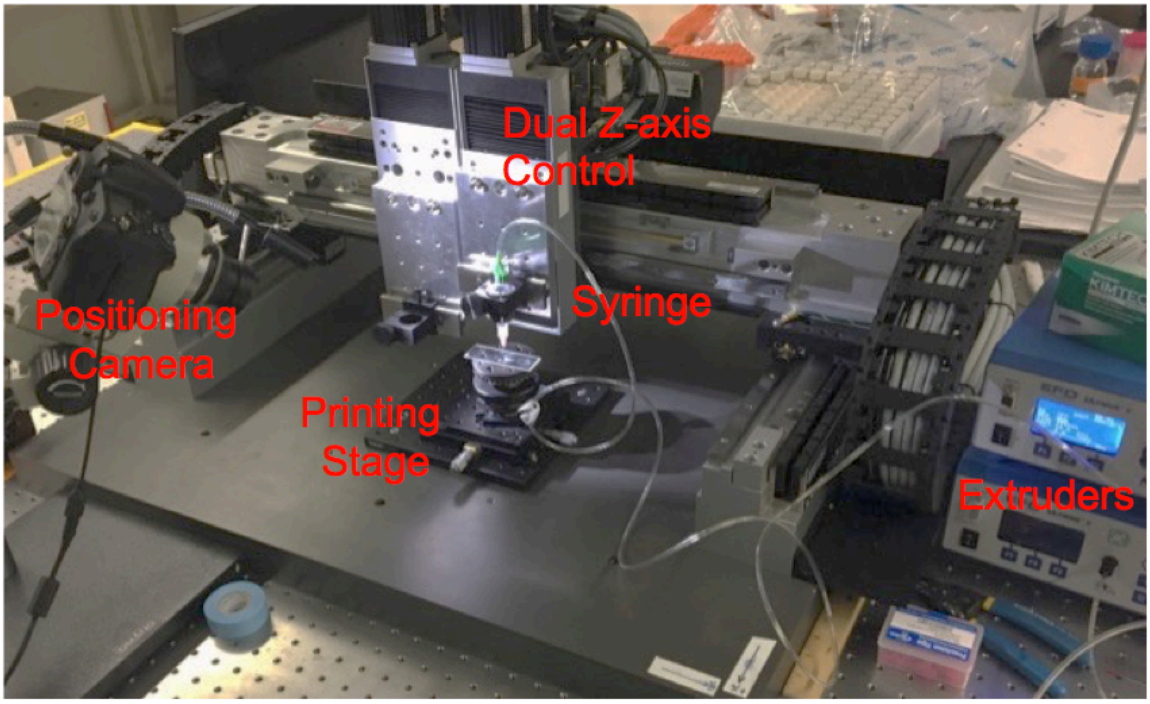

Figure 23. 3D printer setup.

The 3D printing setup is given in Figure 23. Pneumatic pressure applied by the extruder to the printing syringe allows for deposition from the printing syringe onto the glass slide placed onto the printing stage. Positioning of the printing syringe was controlled through the XY-axis gantry and dual Z-axis control. The positioning system was calibrated using the positioning camera. This was input along with the .stl file of the computer aided design (CAD) file to a G-code mapping software (Slic3r). Printing speeds, offsets, nozzle diameters, and support material information was edited and optimized within this software. After complete, the G-code was exported and edited (MATLAB) to be readable by our machine controller (AEROTECH). The 3D printer syringes were loaded with the new materials and loaded onto the printer. Prints were

monitored throughout their production to control printing pressure and prevent nozzle blockages.

References

1 Lebaron, H. M., Mcfarland, J. E. & Burnside, O. C. The Triazine Herbicides : A Milestone in the Development of Weed Control Technology. 1-12 (2008).

2 Fawcett, R. S., Cbm, B. R. & Tierney, D. P. The impact of conservation tillage on pesticide runoff into surface water:. *Journal of Soil and Water Conservation* **49**, 126-135 (1994).

3 Wackett, L. P., Shadowsky, M. J., Martinez, B. & Shapir, N. Biodegradation of atrazine and related s-triazine compounds : from enzymes to field studies. *Applied Microbiology and Biotechnology* **58**, 39-45, doi:10.1007/s00253-001-0862-y (2002).

4 Shimabukuro, R. H., Frear, D. S., Swanson, H. R. & Walsh, W. C. Glutathione Conjugation: An Enzymatic Basis for Atrazine Resistance in Corn. *Plant Physiology* **47**, 10-14 (1971).

5 Bohn, T. *et al.* Determination of atrazine and degradation products in Luxembourgish drinking water : origin and fate of potential endocrine-disrupting pesticides. *Food Additives & Contaminants: Part A* **28**, 1041-1054, doi:10.1080/19440049.2011.580012 (2011).

6 WHO. Atrazine in Drinking-Water. **2** (1996).

7 USEPA. Refined Ecological Risk Assessment for Atrazine. (2016).

8 Muir, D. C. G., Yoo, J. Y. & Baker, B. E. Residues of Atrazine and N-deethylated Atrazine in Water from Five Agricultural Watersheds in Quebec. *Archives of Environmental Contamination and Toxicology* **7**, 221-235 (1978).

9 Rohde, W. A., Asmussen, L. E., Hauser, E. W., Hester, M. L. & Allison, H. D. Atrazine Persistence in Soil and Transport in Surface and Subsurface Runoff from Plots in the Coastal Plain of the Southern United States. *Agro-Ecosystems* **7**, 225-238 (1981).

10 Ghidey, F. *et al.* Herbicide transport to surface runoff from a claypan soil: Scaling from plots to fields. *Journal of Soil and Water Conservation* **65**, 168-179, doi:10.2489/jswc.65.3.168 (2010).

11 Triplett, G. B., Conner, B. J. & Edwards, W. M. Transport of Atrazine and Simazine in Runoff From Conventionaland No-Tillage Corn. *Journal of Environment Quality* **7**, 77-84 (1978).

12 USHHS. Toxilogical Profile for Atrazine. (2003).

13 Kettles, M. A., Browning, S. R., Prince, T. S. & Horstman, S. W. Triazine Herbicide Exposure and Breast Cancer Incidence : An Ecologic Study of Kentucky Counties. *Environmental Health Persepectives* **105**, 1222-1227 (1997).

14 Fan, W. *et al.* Atrazine-Induced Aromatase Expression Is SF-1 Dependent : Implications for Endocrine Disruption in Wildlife and Reproductive Cancers in Humans. *Environmental Health Persepectives* **720**, 720-727, doi:10.1289/ehp.9758 (2007).

15 Van Leeuwen, J. A., Waltner-Toews, D., Abernathy, T., Smit, B. & Shoukri, M. Associations between stomach cancer incidence and drinking water contamination with atrazine and nitrate in ... Associations between stomach cancer incidence and

drinking water contamination with atrazine and nitrate in Ontario (Canada) agroecosystems ,. *International Journal of Epidemiology* **28**, 836-840, doi:10.1093/ije/28.5.836 (1999).

16 Rooney, A. A., Matulka, R. A. & Luebke, R. W. Developmental Atrazine Exposure Suppresses Immune Function in Male , but not Female Sprague-Dawley Rats. *Toxicological Sciences* **76**, 366-375, doi:10.1093/toxsci/kfg250 (2003).

17 Coban, A. & Filipov, N. M. Dopaminergic toxicity associated with oral exposure to the herbicide atrazine in juvenile male C57BL / 6 mice. *Journal of Neurochemistry* **100**, 1177-1187, doi:10.1111/j.1471-4159.2006.04294.x (2007).

18 Graymore, M., Stagnitti, F. & Allinson, G. Impacts of atrazine in aquatic ecosystems. *Environment International* **26**, 483-495 (2001).

19 Hayes, T. *et al.* Atrazine-Induced Hermaphroditism at 0 . 1 ppb in American Leopard Frogs (Rana pipiens): Laboratory and Field Evidence. *Environmental Health Persepectives* **111**, 568-575, doi:10.1289/ehp.5932 (2003).

20 Waring, C. P. & Moore, A. The effect of atrazine on Atlantic salmon (Salmo salar) smolts in fresh water and after sea water transfer. *Aquatic Toxicology* **66**, 93-104, doi:10.1016/j.aquatox.2003.09.001 (2004).

21 Ghosh, P. K. & Philip, L. Environmental Significance of Atrazine in Aqueous Systems and Its Removal By Biological Processes: an Overview. *Global NEST Journal* **8**, 159-178 (2006).

22 Pelizzetti, E. *et al.* Photocatalytic degradation of atrazine and other s-triazine herbicides. *Environmental Science & Technology* **24**, 1559-1565, doi:10.1021/es00080a016 (1990).

23 Adams, C. D. & Watson, T. L. Treatability of s-triazine herbicide metabolites using powdered activated carbon. *Journal of Environmental Engineering* **122**, 327-330 (1996).

24 Chang, S.-W., Lee, S.-J. & Je, C.-H. Phytoremediation of Atrazine by Poplar Trees: Toxicity, Uptake, and Transformation. *Journal of Environmental Science and Health, Part B* **40**, 801-811, doi:10.1080/03601230500227483 (2006).

25 Newcombe, D. A. & Crowley, D. E. Bioremediation of atrazine-contaminated soil by repeated applications of atrazine-degrading bacteria. *Applied Microbiology and Biotechnology* **51**, 877-882, doi:10.1007/s002530051477 (1999).

26 Mutlu, B. R., Yeom, S., Tong, H.-W., Wackett, L. P. & Aksan, A. Silicon alkoxide cross-linked silica nanoparticle gels for encapsulation of bacterial biocatalysts. *Journal of Materials Chemistry A* **1**, 11051, doi:10.1039/c3ta12303k (2013).

27 Struthers, J. K., Jayachandran, K. & Moorman, T. B. Biodegradation of Atrazine by Agrobacterium radiobacter J14a and Use of this Strain in Bioremediation of Contaminated Soil. *Applied and Environmental Microbiology* **64**, 3368-3375 (1998).

28 Souza, M. L. D., Sadowsky, M. J. & Wackett, L. P. Atrazine chlorohydrolase from Pseudomonas sp . strain ADP : gene sequence , enzyme purification , and protein characterization . Atrazine Chlorohydrolase from Pseudomonas sp . Strain

ADP : Gene Sequence , Enzyme Purification , and Protein Characterization. *Journal of Bacteriology* **178**, 4894-4900 (1996).

29 Fan, X. & Song, F. Bioremediation of atrazine: recent advances and promises. *Journal of Soils and Sediments* **14**, 1727-1737, doi:10.1007/s11368-014-0921-5 (2014).

30 Cassidy, M. B., Lee, H. & Trevors, J. T. Environmental applications of immobilized microbial cells: A review. *Journal of Industrial Microbiology* **16**, 79-101, doi:10.1007/BF01570068 (1996).

31 Sultana, K. *et al.* Encapsulation of probiotic bacteria with alginate-starch and evaluation of survival in simulated gastrointestinal conditions and in yoghurt. *International Journal of Food Microbiology* **62**, 47-55, doi:10.1016/S0168-1605(00)00380-9 (2000).

32 Nassif, N. *et al.* Living bacteria in silica gels. *Nature materials* **1**, 42-44, doi:10.1038/nmat709 (2002).

33 Salalha, W., Kuhn, J., Dror, Y. & Zussman, E. Encapsulation of bacteria and viruses in electrospun nanofibres. *Nanotechnology* **17**, 4675-4681, doi:10.1088/0957-4484/17/18/025 (2006).

34 Branyik, T., Kuncova, G., Paca, J. & Demnerova, K. Encapsulation of microbial cells into silica gel. *Journal of Sol-Gel Science and Technology 13* **287**, 283-287, doi:10.1023/A:1008655623452 (1998).

35 Livage, J., Coradin, T. & Roux, C. Encapsulation of biomolecules in silica gels. *Journal of Physics: Condensed Matter* **13**, R673-R691, doi:10.1088/0953-8984/13/33/202 (2001).

36 Hench, L. L. & West, J. K. The sol-gel process. *Chemical Reviews* **90**, 33-72, doi:10.1021/cr00099a003 (1990).

37 Wong, K. V. & Hernandez, A. A Review of Additive Manufacturing. *ISRN Mechanical Engineering* **2012**, 1-10, doi:10.5402/2012/208760 (2012).

38 Gross, B. C., Erkal, J. L., Lockwood, S. Y., Chen, C. & Spence, D. M. Evaluation of 3D printing and its potential impact on biotechnology and the chemical sciences. *Analytical Chemistry* **86**, 3240-3253, doi:10.1021/ac403397r (2014).

39 Johnson, B. N. *et al.* 3D Printed Anatomical Nerve Regeneration Pathways. *Advanced Functional Materials* **25**, 6205-6217, doi:10.1002/adfm.201501760 (2015).

40 Rengier, F. *et al.* 3D printing based on imaging data: Review of medical applications. *International Journal of Computer Assisted Radiology and Surgery* **5**, 335-341, doi:10.1007/s11548-010-0476-x (2010).

41 Mannoor, M. S. *et al.* A 3D Printed Bionic Ear. *Nano Letters*, 23, doi:10.1021/nl4007744 (2013).

42 Kong, Y. L., Gupta, M. K., Johnson, B. N. & McAlpine, M. C. 3D printed bionic nanodevices. *Nano Today* **11**, 330-350, doi:10.1016/j.nantod.2016.04.007 (2016).

43 Lehner, B. A. E., Schmieden, D. T. & Meyer, A. S. A straightforward approach for 3D bacterial printing. *ACS Synthetic Biology*, acssynbio.6b00395, doi:10.1021/acssynbio.6b00395 (2017).

44 Dosier, G. K. Methods for Making Construction Material Using Enzyme Producing Bacteria. (2011).
45 Connell, J. L., Ritschdorff, E. T., Whiteley, M. & Shear, J. B. 3D printing of microscopic bacterial communities. *Proceedings of the National Academy of Sciences of the United States of America* **110**, 18380-18385, doi:10.1073/pnas.1309729110 (2013).
46 Duoss, E. B., Twardowski, M. & Lewis, J. A. Sol-gel inks for direct-write assembly of functional oxides. *Advanced Materials* **19**, 3485-3489, doi:10.1002/adma.200701372 (2007).
47 Chia, H. N. & Wu, B. M. Recent advances in 3D printing of biomaterials. *Journal of Biological Engineering* **9**, 1-14, doi:10.1186/s13036-015-0001-4 (2015).
48 Mutlu, B. R. *et al.* Silica ecosystem for synergistic biotransformation. *Scientific Reports* **6**, 27404, doi:10.1038/srep27404 (2016).
49 Reátegui, E. *et al.* Silica gel-encapsulated AtzA biocatalyst for atrazine biodegradation. *Applied Microbiology and Biotechnology* **96**, 231-240, doi:10.1007/s00253-011-3821-2 (2012).
50 Kauffmann, C. & Mandelbaum, R. T. Entrapment of atrazine chlorohydrolase in sol – gel glass matrix. *Journal of Biotechnology* **62**, 169-176 (1998).
51 Rutz, A. L., Hyland, K. E., Jakus, A. E., Burghardt, W. R. & Shah, R. N. A multimaterial bioink method for 3D printing tunable, cell-compatible hydrogels. *Advanced Materials* **27**, 1607-1614, doi:10.1002/adma.201405076 (2015).
52 Kotz, F. *et al.* Three-dimensional printing of transparent fused silica glass. *Nature* **544**, 337-339, doi:10.1038/nature22061 (2017).
53 Mandelbaum, R. T., Allan, D. l. & Wackett, L. P. Isolation and Characterization of a Pseudomonas sp . That Mineralizes the s -Triazine Herbicide Atrazine. *Applied and environmental microbiology* **61**, 1451-1457 (1995).
54 Shapir, N., Osborne, J. P., Johnson, G., Sadowsky, M. J. & Wackett, L. P. Purification, substrate range, and metal center of AtzC: The N-isopropylammelide aminohydrolase involved in bacterial atrazine metabolism. *Journal of Bacteriology* **184**, 5376-5384, doi:10.1128/JB.184.19.5376-5384.2002 (2002).
55 De Souza, M., Wackett, L. P., Boundy-Mills, K. L., Mandelbaum, R. T. & Sadowsky, M. J. Cloning, characterization, and expression of a gene region from Pseudomonas sp. strain ADP involved in the dechlorination of atrazine. *Applied and Environmental Microbiology* **61**, 3373-3378 (1995).
56 Strong, L. C., McTavish, H., Sadowsky, M. J. & Wackett, L. P. Field-scale remediation of atrazine-contaminated soil using recombinant Escherichia coli expressing atrazine chlorohydrolase. *Environmental Microbiology* **2**, 91-98, doi:10.1046/j.1462-2920.2000.00079.x (2000).
57 Ali Khan, A. & Alzohairy, M. a. Recent Advances and Applications of Immobilized Enzyme Technologies: A Review. *Research Journal of Biological Sciences* **5**, 565-575, doi:10.3923/rjbsci.2010.565.575 (2010).
58 De Vos, P., Lazarjani, H. A., Poncelet, D. & Faas, M. M. Polymers in cell encapsulation from an enveloped cell perspective. *Advanced Drug Delivery Reviews* **67-68**, 15-34, doi:10.1016/j.addr.2013.11.005 (2014).

59 Callone, E., Campostrini, R., Carturan, G., Cavazza, A. & Guzzon, R. Immobilization of yeast and bacteria cells in alginate microbeads coated with silica membranes: procedures, physico-chemical features and bioactivity. *Journal of Materials Chemistry* **18**, 4839-4848, doi:10.1039/b807301e (2008).
60 Dave, B. C., Dunn, B., Valentine, J. S. & Zink, J. I. Sol-gel encapsulation methods for biosensors. *Analytical Chemistry* **66**, 1120A-1127A, doi:10.1021/ac00094a001 (1994).
61 Avnir, D., Braun, S., Lev, O. & Ottolenghi, M. Enzymes and Other Proteins Entrapped in Sol-Gel Materials. *Chemistry of Materials* **6**, 1605-1614, doi:10.1021/cm00046a008 (1994).
62 Gill, I. & Ballesteros, A. Bioencapsulation within synthetic polymers (Part 1): sol gel encapsulated biologicals. *Trends in Biotechnology* **18**, 282-296, doi:10.1016/s0167-7799(00)01457-8 (2000).
63 Carturan, G., Dal Toso, R., Boninsegna, S. & Dal Monte, R. Encapsulation of functional cells by sol-gel silica: actual progress and perspectives for cell therapy. *Journal of Materials Chemistry* **14**, 2087-2098, doi:Doi 10.1039/B401450b (2004).
64 Ko, E. in *Preparation of Solid Catalysts* 85-98 (1999).
65 Sakkos, J. K., Kieffer, D. P., Mutlu, B. R., Wackett, L. P. & Aksan, A. Engineering of a silica encapsulation platform for hydrocarbon degradation using Pseudomonas sp . NCIB 9816-4. *Biotechnology and Bioengineering* **9999**, n/a-n/a, doi:10.1002/bit.25821 (2015).
66 Ponton, a., Warlus, S. & Griesmar, P. Rheological study of the sol-gel transition in silica alkoxides. *Journal of colloid and interface science* **249**, 209-216, doi:10.1006/jcis.2002.8227 (2002).
67 Shchipunov, Y. A., Kojima, A. & Imae, T. Polysaccharides as a template for silicate generated by sol-gel processes. *Journal of Colloid and Interface Science* **285**, 574-580, doi:10.1016/j.jcis.2004.11.026 (2005).
68 Salama, A. & Salama, A. Polysaccharides / silica hybrid materials : New perspectives for sustainable raw materials Polysaccharides / silica hybrid materials : New perspectives for sustainable raw materials. *Journal of Carbohydrate Chemistry* **35**, 131-149, doi:10.1080/07328303.2016.1154152 (2017).
69 Davis, E. M. & Davis, R. J. Fundamentals of Chemical Reaction Engineering. *Journal of Chemical Education* **43**, 384, doi:10.1021/ed043pA758.1 (2003).
70 Mutlu, B. R., Yeom, S., Wackett, L. P. & Aksan, A. Modelling and optimization of a bioremediation system utilizing silica gel encapsulated whole-cell biocatalyst. *Chemical Engineering Journal* **259**, 574-580, doi:10.1016/j.cej.2014.07.130 (2015).
71 Zaslaver, A. *et al.* A comprehensive library of fluorescent transcriptional reporters for Escherichia coli. *Nature methods* **3**, 623-628, doi:10.1038/nmeth895 (2006).
72 Callister, W. D. J. & Rethwisch, D. G. Materials science and engineering: an introduction. *Materials Science and Engineering* **94**, 266-267, doi:10.1016/0025-5416(87)90343-0 (2007).

73 Crank, J. The Mathematics of Diffusion. 414, doi:10.1016/0306-4549(77)90072-X (1975).
74 Eiselt, P., Yeh, J., Latvala, R. K., Shea, L. D. & Mooney, D. J. Porous carriers for biomedical applications based on alginate hydrogels. *Biomaterials* **21**, 1921-1927, doi:10.1016/S0142-9612(00)00033-8 (2000).
75 Munson, B. R., Okiishi, T. H., Huebsch, W. W. & Rothmayer, A. P. Fundamentals of Fluid Mechanics. **16**, 227-228, doi:10.1016/0378-3804(88)90174-X (1988).

Appendix A

χ^2 MATLAB Code

```
% Input Variables
numPoints=length(XM);
xRange=511;
yRange=510;
zRange=101;

% Choose # bins Freedman-Diaconis Rule
xnumofbins=round(xRange/(2*iqr(XM)*numPoints^(-1/3)));
ynumofbins=round(yRange/(2*iqr(YM)*numPoints^(-1/3)));
znumofbins=round(zRange/(2*iqr(ZM)*numPoints^(-1/3)));

% Putting into bins
xinbins=floor(XM/(xRange/xnumofbins))+1;
yinbins=floor(YM/(yRange/ynumofbins))+1;
zinbins=floor(ZM/(zRange/znumofbins))+1;
counts=accumarray({xinbins,yinbins,zinbins,1,[]);
prodbinnums=xnumofbins*ynumofbins*znumofbins;

% Calc x2 stat
x2=(counts-numPoints/prodbinnums).^2/(numPoints/prodbinnums);
calcchi2value=sum(x2(:))

%Calc threshold x2 - critical value
chi2threshold=chi2inv(0.95,prodbinnums-1)

%If test
if calcchi2value < chi2threshold
   Teststmt=sprintf('PASS: Test cannot confirm that distribution is non-uniform')
else
   Teststmt=sprintf('FAIL: Test confirms distribution is non-uniform')
end

%Calc p value (% chance that saying dist is non-uniform is incorrect)
pvalue=1-chi2cdf(calcchi2value,prodbinnums-1);
sprintf('%0.4f', pvalue)

%Intensity map
imagesc(sum(counts,3))
colorbar
```